processes

MDPI

Article

Numerical Study on the Transient Pneumatic Characteristics of a Piston-Type Air Compressor During the Compressing Process

Yan-Juan Zhao [1], Bing-Yin Zhou [2], Hui-Fan Huang [3,*], Wan-Wan Tian [4], Yan-Jie Wang [1], Hai-Bin Lin [5], Liang-Huai Tong [5,*] and Yu-Liang Zhang [4,*]

[1] College of Information Engineering, Quzhou College of Technology, Quzhou 324000, China; zyj@qzct.edu.cn (Y.-J.Z.)
[2] State Grid Corporation of China United Pipeline Co., Ltd., West East Gas Pipeline Branch, Yangzhou 225100, China
[3] School of Mechanical Engineering, Hunan University of Technology, Zhuzhou 412007, China
[4] College of Mechanical Engineering, Quzhou University, Quzhou 324000, China
[5] Quzhou Academy of Metrology and Quality Inspection, Quzhou 324024, China
* Correspondence: m23080200011@stu.hut.edu.cn (H.-F.H.); tonglh2000@163.com (L.-H.T.); zhang002@sina.com (Y.-L.Z.); Tel.: +86-158-5700-3926 (Y.-L.Z.)

Abstract: To investigate the pneumatic characteristics of a piston-type air compressor during the rapid transient processes of intake and compression, this study establishes a computational model incorporating the tank, valves, cylinder, intake and discharge pipe, etc. Utilizing the dynamic mesh method combined with user-defined functions, numerical calculations were performed to analyze the compression process, focusing on pressure variation patterns at various positions inside the cylinder and their impact on compressor performance. The purpose is to enhance understanding of these dynamics. Key findings reveal that during the intake phase, pressure at all monitored points rapidly decreases, with the most significant pressure changes occurring directly below the intake valve. Pressure variations on the surfaces of the intake and discharge valves exhibit high consistency. However, during compression, negative pressure changes become more pronounced. The pressures on the top, side walls, and bottom of the cylinder rapidly decrease as the compression ends. Furthermore, as air flows into the storage tank, its pressure decreases but remains mostly stable until equilibrium is reached, causing the tank pressure to rise. Finally, significant low-pressure areas were observed in small corners below the pipe, while higher pressure values were found in larger corners above the side, demonstrating flow characteristics and energy loss under different geometric conditions.

Keywords: piston-type compressor; compressing process; dynamic mesh; numerical simulation; pressure characteristics

check for updates

Academic Editor: Krzysztof Rogowski

Received: 6 March 2025
Revised: 5 April 2025
Accepted: 15 April 2025
Published: 16 April 2025

Citation: Zhao, Y.-J.; Zhou, B.-Y.; Huang, H.-F.; Tian, W.-W.; Wang, Y.-J.; Lin, H.-B.; Tong, L.-H.; Zhang, Y.-L. Numerical Study on the Transient Pneumatic Characteristics of a Piston-Type Air Compressor During the Compressing Process. *Processes* **2025**, *13*, 1211. https://doi.org/10.3390/pr13041211

Copyright: © 2025 by the authors. Licensee MDPI, Basel, Switzerland. This article is an open access article distributed under the terms and conditions of the Creative Commons Attribution (CC BY) license (https://creativecommons.org/licenses/by/4.0/).

1. Introduction

Piston-type air compressors, characterized by their high efficiency and reliability, have found widespread application across various fields. Their performance is directly influenced by multiple factors such as temperature, pressure, and moisture content; changes in these variables can directly impact the compressor's efficiency and service life. Therefore, an in-depth investigation into the working mechanism of piston-type air compressors and the characteristics of internal fluid flow is critical for optimizing design and enhancing performance. The study conducted by I. K. Shatalov et al. specifically focused on the roles of temperature and pressure during the initial stages of the compression process. They found that temperature variations in the early phase were primarily caused by the

heating of the gas through wall surfaces and its moisture content, while pressure changes predominantly depended on piston speed and the gas's moisture content. The research revealed that the rise in temperature and decline in pressure served as the primary causes for reduced air supply and decreased efficiency in compressors [1]. This conclusion lays a theoretical foundation for subsequent research and provides guidance, especially in addressing issues through design optimization.

With the advancement of technology, Computational Fluid Dynamics (CFD) has become a powerful tool for studying the internal flow characteristics of compressors. Selvaraj et al.'s research utilized topology optimization and metal 3D printing technology to design a more efficient air compressor piston. This innovation not only saved material but also improved the overall efficiency of the compressor, opening new paths for the design optimization of other components [2]. The successful implementation of this design method demonstrates the enormous potential of modern technology in enhancing compressor performance. Meanwhile, the lubrication system of the compressor is also a critical factor influencing its performance. Fritz et al. proposed a comprehensive lubrication model that takes into account the complex interactions between the oil film, compressed gas, piston and its guide rings, piston movement, bending of the piston rod, and crosshead motion, aiming to find the most optimized lubrication strategy [3]. The model fills the gap in the field of piston compressor lubrication research and points the way towards improving the long-term stability and reliability of compressors.

To further enhance the efficiency of compressors, researchers have explored a variety of improvement measures. Khaljani et al., through experimental and modeling analysis, used aluminum parallel plates of varying heights as heat exchangers, successfully improving the compression efficiency of hydraulic piston gas compressors [4]. Khait et al. developed and validated a strongly coupled thermodynamic and heat exchange model for a hybrid piston compressor with regenerative heat exchange. They introduced a multi-timescale numerical model not constrained by the geometric limitations of the heat exchange section domain for the first time, finding that heating during compressor operation can lead to reduced energy efficiency, whereas regenerative heat exchange helps to overcome this limitation [5]. Silva et al., through simulation models, predicted and achieved significant improvements in thermodynamic and volumetric efficiency, providing concrete solutions for enhancing compressor efficiency and pointing the way for future technological advancements [6].

Furthermore, the thermodynamic behavior of gas compressors has also attracted considerable attention. Taleb et al.'s research revealed the differences in the performance of real gases compared to ideal gases within a gas spring, underscoring the importance of selecting an appropriate gas model, which is crucial for accurately predicting compressor performance [7]. The experimental study by Patil et al. showed that using water-based foam can effectively reduce the temperature of air during compression, thereby enhancing isothermal compression efficiency [8]. They further explored the impact of compression rate on the heat transfer rate and the potential to minimize efficiency fluctuations through optimized foam generator design [9]. These studies provide valuable insights into improving the thermal efficiency of compressors.

Regarding the convective heat transfer characteristics within compressors, the experimental analysis by Neu et al. provided important data support for understanding the convection heat transfer patterns of hydraulic piston compressed air in large-volume chambers [10]. Through experiments and a thermal resistance circuit model, Patil et al. analyzed the heat transfer mechanisms during air compression in hydraulic piston compressors. They found that the faster the compression speed, the higher the heat transfer rate; however, this also leads to increased compression power consumption and air temperature. The convective heat transfer coefficient of the air rapidly decreases as the compression progresses

and tends to stabilize towards the end of the compression process. Different materials used for the compression chamber significantly influence the initial heat transfer coefficients. Hydraulic pistons achieved an isothermal compression efficiency of 84–86% [11]. These studies collectively deepen our understanding of the internal physical processes within compressors and lay a solid theoretical foundation for future optimized design.

Niazmand et al. compiled a numerical analysis to study the variation in thermodynamic efficiency of reciprocating compressors at different angular velocities, finding that as the angular velocity increases, so does the entropy generation, leading to a decrease in the compressor's efficiency and isentropic efficiency [12]. Farzaneh-Gord et al., through a theoretical analysis model, compared the performance of ideal gas models with real gas models in natural gas reciprocating compressors. The results showed that although the control volume temperature is lower under the real gas model, the mass flow rate and energy consumption are both higher [13]. Leandro R. Silva et al. focused on the issue of gas leakage in small reciprocating compressors when reed valves do not seal completely, indicating that even a very small valve clearance can significantly impact compressor efficiency, particularly noting that discharge valve leakage affects efficiency much more than intake valve leakage [14]. Wang et al. proposed a non-destructive testing method based on strain gauges for monitoring dynamic pressure in hydraulically driven piston compressors. This method not only determined the optimal monitoring points through finite element analysis but was also validated on a two-stage hydraulically driven piston compressor [15].

Kong et al. proposed a dual-piston two-stage linear CO_2 compressor, and through the analysis of its dynamic characteristics, they found that this design can effectively reduce the average gas force, improve compression efficiency, and decrease leakage during the compression process [16]. Ye et al. established a three-dimensional numerical model for a hydraulically driven piston hydrogen compressor, studying in depth the effects of valve opening and closing on pressure fluctuations within the cylinder and temperature distribution, emphasizing the importance of heat transfer during the compression phase [17]. Wu et al., through a three-dimensional fluid–structure coupling model, analyzed in detail the oscillatory motion of the intake valve mounted on the piston, showing that such a design can enhance the reliability and efficiency of the compressor [18]. Zhou introduced a multi-stage hydraulic piston compressor specifically designed for hydrogen compression, addressing issues of operational instability and low compression efficiency in traditional compressors by designing a buffer structure [19]. Xu et al. proposed an isothermal piston structure aimed at enhancing heat exchange between air and the environment via a gas–solid–liquid three-layer heat transfer structure and porous media, thereby achieving isothermal compression and significantly improving compression efficiency [20]. Han et al. proposed a new type of hydraulic piston adiabatic compressed air energy storage system, which not only improved the round-trip efficiency of the system but also enhanced the flexibility and multipower output capability of the system by optimizing the number of compressor stages and pressure ratio distribution [21].

In the field of compressor control and regulation, Wang et al. developed an improved continuous capacity modulation numerical model for reciprocating compressors, analyzing the impact of key parameters such as hydraulic force, displacement, and velocity of the unloader, and proposed optimization solutions to achieve minimum power consumption [22]. Gao et al. adopted the Analytic Hierarchy Process (AHP) to construct a quality evaluation system for large-scale piston compressor manufacturing enterprises, providing a scientific basis for improving propipe quality and management levels [23]. Hu et al. introduced a novel screw compressor specifically designed for large-scale hydrogen liquefaction, achieving high efficiency and low noise and low vibration operation effects by

optimizing the dynamic performance of the rotors [24]. Wang et al., through establishing a simplified fluid–structure coupling model, analyzed the dynamic stress of the discharge valve plate in supercritical CO_2 compressors, providing theoretical support for enhancing the safety and reliability of compressors [25]. Zhi et al. used complex vector methods to graphically analyze the output pressure amplitude of high-performance linear compressors, proposing methods to increase the output pressure amplitude, which is beneficial for the miniaturization design of compressors [26]. Ma et al. proposed an automated compressor performance mapping method based on artificial neural networks (ANNs), demonstrating its advantages over traditional models and applicability to various types of compressors [27]. Due to the degradation of compressor performance caused by valve dynamics, D. Taranović et al. proposed a mathematical model to predict valve dynamics, which was validated through thermodynamic tests on a reciprocating compressor used in motor vehicles [28]. Additionally, concerning the significant mechanical wear in piston air compressors caused by reciprocating motion, scholars like Saša Milojević conducted in-depth research on tribological factors. Their study explains how parameters such as sliding speed, contact time, and contact area affect friction and wear in materials under relative motion, providing theoretical support for selecting suitable materials for piston air compressors [29]. These research findings collectively advance the technology of reciprocating compressors, providing important references for improving their efficiency, reliability, and scope of application. While substantial research exists regarding bulk thermodynamic measurements, critical knowledge gaps persist in characterizing real-time spatial pressure variations during dynamic operational states.

In summary, the performance optimization of piston air compressors involves complex multidisciplinary knowledge. With the aid of CFD's simulation technology, a deeper understanding of the fluid characteristics within the compressor can be achieved, thereby providing a scientific basis for design optimization. Nevertheless, existing studies frequently neglect a comprehensive examination of the internal pressure field characteristics in linear air compressors, a crucial factor for enhancing efficiency and reliability. To bridge this research gap, the present investigation delves into the distinct pressure distribution dynamics inherent to these systems.

This study aims to simulate the compression process of a piston air compressor using CFD Fluent software (version 2020 R2), exploring the fluid characteristics involved, to provide theoretical support and technical guidance for further optimization of compressor design.

2. Computational Model and Method

2.1. Physical Model

Figure 1 shows the main components of a piston air compressor. This compressor consists of six core parts: intake pipe, discharge pipe, storage tank, cylinder, intake valve, and exhaust valve. During the suction phase, the piston moves downward, causing the intake valve to open, thereby allowing air to be drawn into the cylinder from the intake pipe, while the exhaust valve remains closed. In the compression phase, as the piston moves upward, it compresses the air inside the cylinder. During this stage, the intake valve is actively closed, and the exhaust valve is actively opened, enabling the compressed air to be pushed through the discharge pipe and into the storage tank for future use. This cyclic process, driven by the active operation of the valves and the reciprocating motion of the piston, ensures a continuous supply of compressed air.

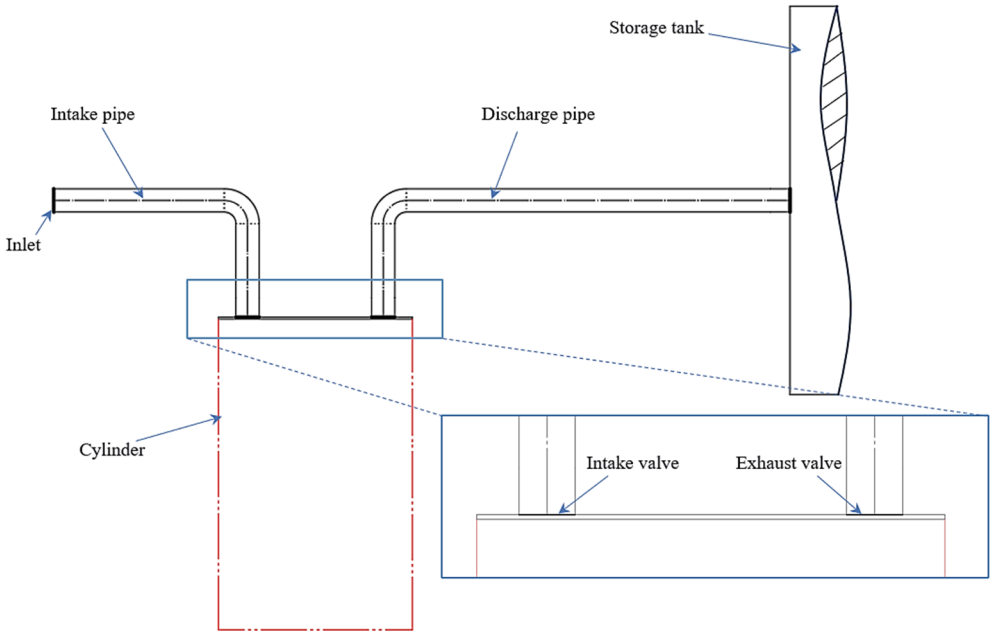


Figure 1. The composition of a piston-type air compressor.

Figure 2 shows the dimensions of the computational domain. In the figure, the red lines mark the area where the piston moves throughout its entire stroke. With this view, the exact scope of the computational domain and the boundary conditions of the piston's motion path are clearly presented.

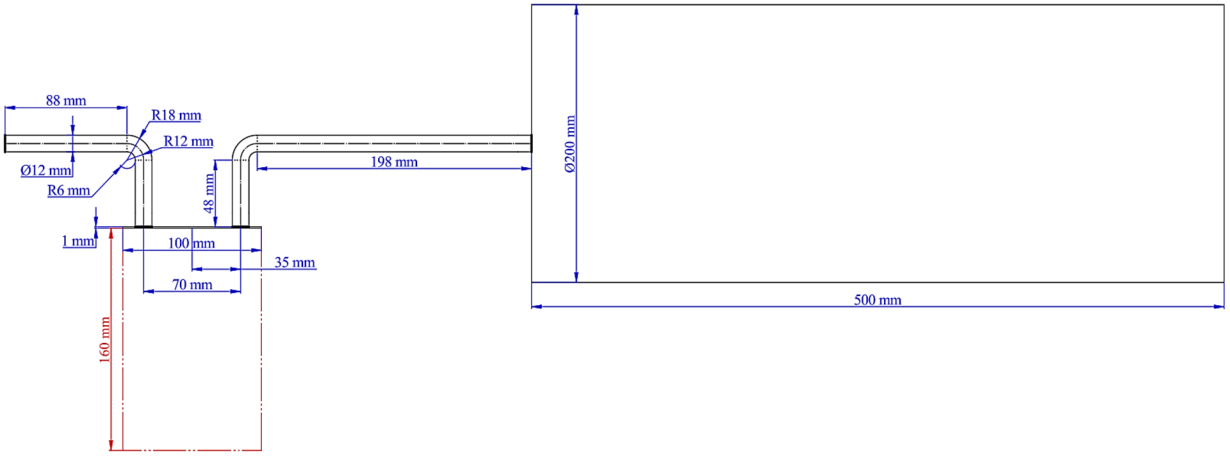


Figure 2. Schematic of computational domain dimensions.

When the piston is at the Top Dead Center (TDC) position, as shown in Figure 3. This state marks the initial moment of the numerical calculation, defined as time $t = 0$ s. At this point, the piston is located at the highest position of its stroke.

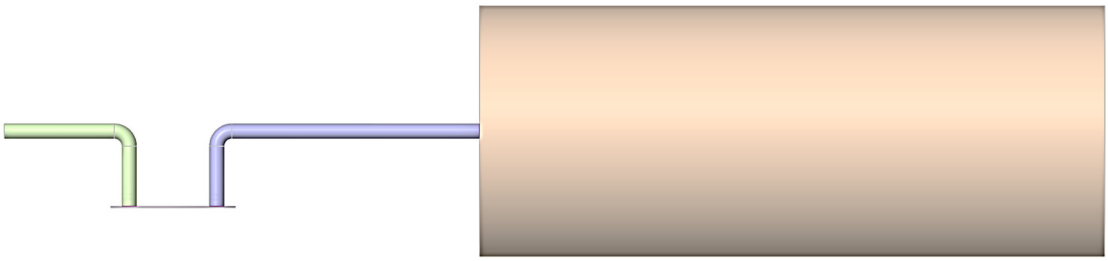


Figure 3. Fluid domain when the piston is at TDC.

When the piston reaches the Bottom Dead Center (BDC) position, as shown in Figure 4. This moment represents another significant time point in the calculation process, which is at t = 0.01 s. At this position, the piston is at the lowest point of its stroke.

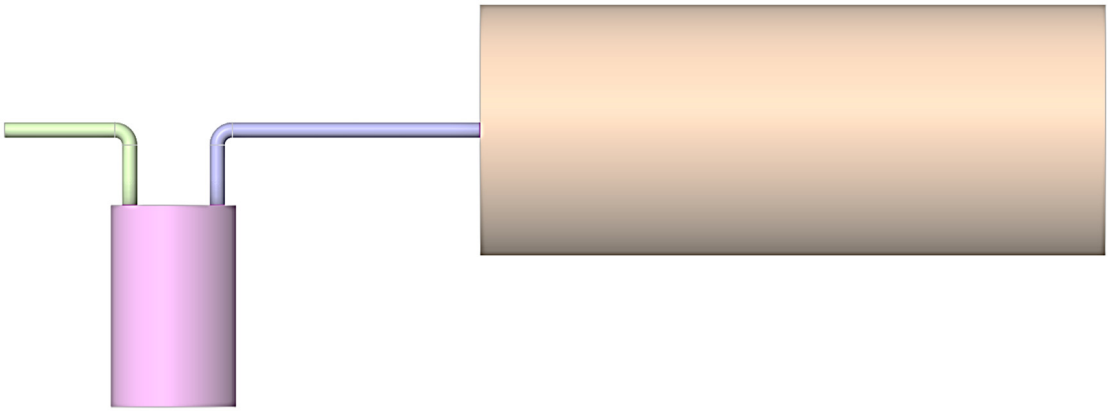


Figure 4. Fluid domain when the piston is at BDC.

2.2. Calculating Scheme

The direction of the piston moving from the TDC to the BDC is defined as the positive direction, with the displacement being 0 m when the piston is at the TDC position and 160 mm when it is at the BDC position. Piston displacement function:

$$x = 80\sin(100\pi t - \frac{\pi}{2}) + 80 \quad (1)$$

The function graph is shown in Figure 5.

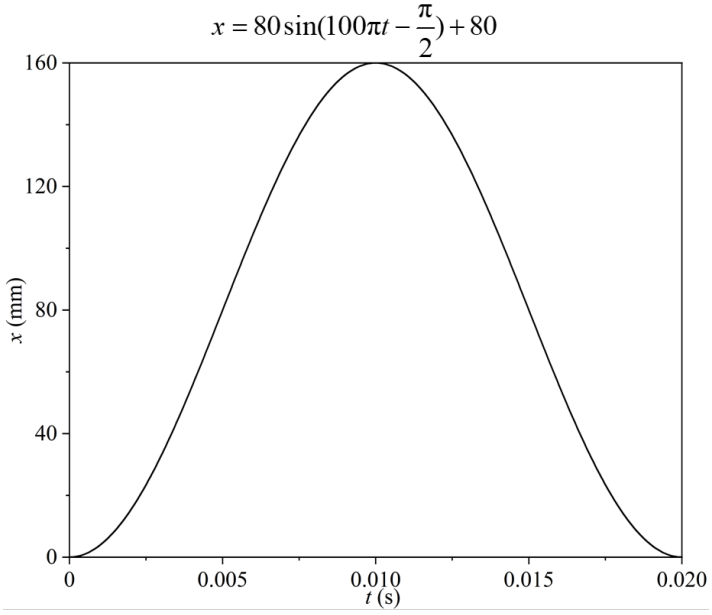


Figure 5. Piston operation displacement diagram.

Define the direction of the piston moving from the TDC downwards to the BDC as a positive direction. Under this setting, when the piston is at TDC, its displacement value is 0 m, and when the piston reaches BDC, the displacement amount is positively 160 mm. According to the above definition, the pattern of displacement changes throughout the stroke of the piston can be visually demonstrated by the displacement–time function graph shown in Figure 5.

The velocity characteristics of the piston at different time points are described by the velocity–time function graph presented in Figure 6.

$$v = 8000\pi \sin(100\pi t) \tag{2}$$

Specific function graph is shown in Figure 6.

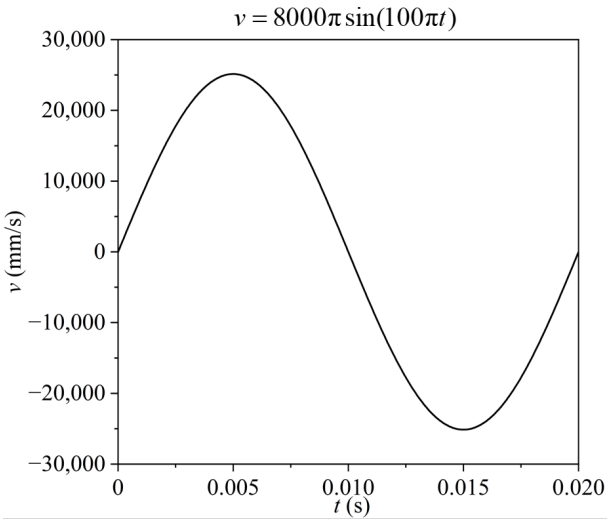


Figure 6. Piston operation velocity diagram.

2.3. Boundary Conditions and Setup

The bottom of the cylinder is set as the piston face, which is the moving surface of the dynamic mesh; the intake manifold port is set as a pressure inlet; the intake valve is defined as an internal fluid region during the intake process and changed to a wall during the compression process; the exhaust valve is set as a wall during the intake process and changed to an internal fluid region during the compression process; and all other surfaces are set as walls. In the initial state, the pressure inside the intake manifold and the cylinder is 101,325 Pa, while the pressure in the exhaust manifold and the reservoir is 400,000 Pa. The calculation steps are set to 400 steps with a time step size of 0.00005 s, and the maximum stretch height of the dynamic mesh is set to 0.5 mm.

2.4. Numerical Method

In this study of compressible fluid dynamics, the Navier–Stokes (NS) equations in cylindrical coordinates are used to describe the motion of fluids and momentum changes within fluid motion [30].

Radial momentum equation:

$$\rho\left(u\frac{\partial u}{\partial r} + v\frac{\partial u}{\partial \theta} + w\frac{\partial u}{\partial z} - \frac{v^2}{r}\right) = -\frac{\partial p}{\partial r} + \mu\left[\frac{1}{r}\frac{\partial}{\partial r}\left(r\frac{\partial u}{\partial r}\right) + \frac{1}{r^2}\frac{\partial^2 u}{\partial \theta^2} + \frac{\partial^2 u}{\partial z^2} - \frac{u}{r^2} - \frac{2}{r^2}\frac{\partial v}{\partial \theta}\right] + F_r \tag{3}$$

Circumferential (or tangential) momentum equation:

$$\rho\left(u\frac{\partial v}{\partial r} + v\frac{\partial v}{\partial \theta} + w\frac{\partial v}{\partial z} - \frac{uv}{r}\right) = -\frac{1}{r}\frac{\partial p}{\partial \theta} + \mu\left[\frac{1}{r}\frac{\partial}{\partial r}\left(r\frac{\partial v}{\partial r}\right) + \frac{1}{r^2}\frac{\partial^2 v}{\partial \theta^2} + \frac{\partial^2 v}{\partial z^2} + \frac{2}{r^2}\frac{\partial u}{\partial \theta} - \frac{v}{r^2}\right] + F_\theta \tag{4}$$

Axial momentum equation:

$$\rho\left(u\frac{\partial w}{\partial r} + v\frac{\partial w}{\partial \theta} + w\frac{\partial w}{\partial z}\right) = -\frac{\partial p}{\partial z} + \mu\left[\frac{1}{r}\frac{\partial}{\partial r}\left(r\frac{\partial w}{\partial r}\right) + \frac{1}{r^2}\frac{\partial^2 w}{\partial \theta^2} + \frac{\partial^2 w}{\partial z^2}\right] + F_z \tag{5}$$

where ρ is the fluid density; u, v, and w are the velocity components in the radial, circumferential (or tangential), and axial directions, respectively; p is the pressure; μ is the dynamic viscosity; and F_r, F_θ, and F_z are the body forces in the radial, circumferential, and axial directions, respectively.

Furthermore, the energy equation describes the transformation between internal and kinetic energy within the fluid and the transport of energy [30].

$$\rho c_p \left(u\frac{\partial T}{\partial r} + v\frac{\partial T}{\partial \theta} + w\frac{\partial T}{\partial z} \right) = k\left(\frac{1}{r}\frac{\partial}{\partial r}\left(r\frac{\partial T}{\partial r} \right) + \frac{1}{r^2}\frac{\partial^2 T}{\partial \theta^2} + \frac{\partial^2 T}{\partial z^2} \right) + \Phi \quad (6)$$

where c_p is the specific heat capacity; T is the temperature; and k is the thermal conductivity. Φ is the heat source term due to viscous dissipation.

The standard k-ε turbulence model is selected for simulating complex compressor flows due to its well-established validation in similar applications, demonstrated numerical stability, and reliable performance in capturing key flow features [30,31]. The core equations of the standard k-ε model include the turbulent kinetic energy equation and the turbulent dissipation rate equation.

Turbulent kinetic energy equation:

$$\frac{\partial(\rho k)}{\partial t} + \frac{\partial(\rho k u)}{\partial x} + \frac{\partial(\rho k v)}{\partial y} + \frac{\partial(\rho k w)}{\partial z} = +\frac{\partial}{\partial x_j}\left[\left(\mu + \frac{\mu_t}{\sigma_k} \right)\frac{\partial k}{\partial x_j} \right] + P_k + G_b - \rho\varepsilon \quad (7)$$

where $\mu_t = C\mu\frac{k^2}{\varepsilon}$ represents the eddy viscosity; $P_k = \tau_{ij}\frac{\partial u_i}{\partial x_j}$ represents the turbulent kinetic energy caused by mean velocity gradients; G_b refers to the turbulent kinetic energy generated by buoyancy; σ_k is the Prandtl number related to the transport of turbulent kinetic energy; and C_μ is an empirical constant, with a typical value of 0.09.

Turbulent dissipation rate equation:

$$\frac{\partial(\rho\varepsilon)}{\partial t} + \frac{\partial(\rho\varepsilon u)}{\partial x} + \frac{\partial(\rho\varepsilon v)}{\partial y} + \frac{\partial(\rho\varepsilon w)}{\partial z} = \frac{\partial}{\partial x_j}\left[\left(\mu + \frac{\mu_t}{\sigma_\varepsilon} \right)\frac{\partial \varepsilon}{\partial x_j} \right] + C_1\frac{\varepsilon}{k}(P_k + G_b) - C_2\rho\frac{\varepsilon^2}{k} \quad (8)$$

where σ_ε is the Prandtl number associated with the transport of turbulent dissipation rate, and C_1 and C_2 are empirical constants, with typical values of 1.44 and 1.92, respectively.

These equations constitute the core of the standard k-ε turbulence model. By solving these equations, distributions of physical quantities in the flow field can be obtained, such as mean velocity, pressure, and temperature, which facilitates the analysis of flow characteristics within a compressor. In practical applications, for low Reynolds number flows, these equations are typically addressed using a mixed analytical/numerical method: the advection–diffusion components are solved numerically, while the source terms are handled in two parts—one part is resolved analytically and the other part numerically. Numerical methods such as the finite difference method, finite element method, or finite volume method are commonly employed for the numerical solutions.

To implement the operation of the piston, a user-defined function (UDF) compiled independently is imported into the simulation. In the compressor simulation, structured moving mesh technology is utilized to accommodate the motion of the piston [32]. The primary challenge addressed is the deformation of the mesh and the consequent update of the flow field variables. This is achieved using a single fundamental equation for mesh deformation, where the connections between mesh nodes are analogized to springs. By

minimizing the potential energy of these "springs", the mesh deformation is calculated. The fundamental equation is as follows:

$$F_i = \sum_j k_{ij}(x_j - x_i - l_{ij}) \tag{9}$$

where F_i is the force on node i; X_i and X_j are the positions of nodes i and j; l_{ij} is the initial distance between nodes i and j; and k_{ij} is the spring stiffness coefficient.

Once the new positions of the nodes are determined, an explicit Euler method can be used to update the position information of the nodes. The specific calculation is as follows:

$$x_i^{n+1} = x_i^n + \Delta t v_i^n \tag{10}$$

where x_i^{n+1} is the position of node i at step n; v_i^n is the velocity of node i at step n; and Δt is the time step.

After completing the mesh deformation, in order to ensure the continuity and accuracy of the flow field variables on the new mesh, these variables need to be re-interpolated. Using a high-order interpolation method, such as cubic spline interpolation, can significantly improve the accuracy of the interpolation. The expression for this is as follows:

$$\phi(x) = \sum_{i=1}^{N} \phi_i S_i(x) \tag{11}$$

where ϕ_i is the value of the flow field variable at node i, and $S_i(x)$ is the cubic spline interpolation function.

Through these steps, the dynamic flow processes inside an air compressor can be effectively simulated, providing crucial data support for design and optimization.

2.5. Grid Independence

GCI can more accurately assess the convergence of simulation results, avoiding the limitations of evaluating results based solely on a single mesh size. The introduction of GCI allows researchers to better judge the reliability of simulation results and optimize the mesh selection and precision requirements for numerical simulations. GCI is an indicator used to evaluate the convergence of numerical simulation results. It assesses the convergence of simulation results as they approach infinitely small mesh sizes by comparing differences in output quantities across different mesh sizes. The calculation steps for GCI in this paper are as follows [33,34].

The formula for calculating the ratio of the number of grids is expressed as follows:

$$r_{n,n+1} = \left(\frac{N_{n+1}}{N_n}\right)^{\frac{1}{3}} \tag{12}$$

where r is the ratio of mesh cell counts and N is the number of grids.

The formula for obtaining the relative error of computed values is as follows:

$$e_{n,n+1} = \left|\frac{f_n - f_{n+1}}{f_{n+1}}\right| \tag{13}$$

where e the relative error and f is the monitored value.

The formula for calculating GCI is expressed as follows:

$$GCI_{n+1} = C\frac{{e_{n,n+1}}^p}{r_{n,n+1} - 1} \times 100\% \tag{14}$$

where C is a scaling factor used to correct the influence of the error term, typically ranging from 1.25 to 3.00; p is the coefficient of the error term, with a typical range of 1 to 2. In this paper, c is taken as 3, and p is taken as 1.

The criteria for determining GCI values usually depend on the specific numerical computation problem and the methods used. In practice, one can evaluate convergence by using different numerical computation methods for the same problem and comparing their GCI values. However, it is common practice to limit the GCI value within an acceptable range, such as 10% or 5%. That is, when the GCI is less than or equal to 10% or 5%, it can be considered that the computational method has converged.

Verification of grid independence is performed for critical areas (intake pipe, discharge pipe, and cylinder) in Figure 7.

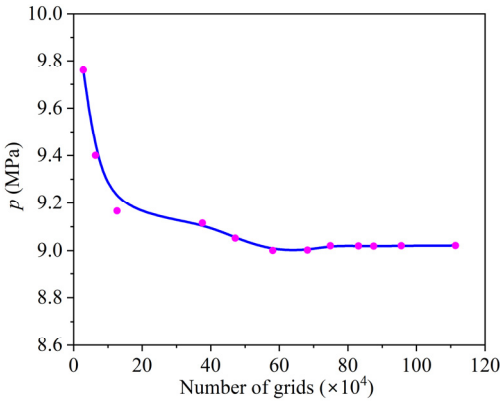


Figure 7. Grid independence verification.

The calculated GCI values are shown in Table 1.

Table 1. Calculated GCI values.

Serial Number	GCI Value
1–2	36.75%
2–3	29.94%
3–4	3.78%
4–5	26.84%
5–6	23.81%
6–7	0.78%
7–8	19.62%
8–9	1.30%
9–10	1.10%
10–11	1.50%
11–12	0.70%

According to the data in the table, it can be observed that the GCI values from entries 8–9 and thereafter are all less than 2%, meeting the previously mentioned criteria. This indicates that after entry number 9, the number of grids of 831,312 has a very minimal effect on the observed values.

Therefore, the number of grid cells in critical areas should be greater than 800,000. The total number of grid cells used for computation is 1,236,295, with 217,224 cells in the tank area and 1,019,071 cells in other critical areas. The final mesh division is illustrated in Figure 8.

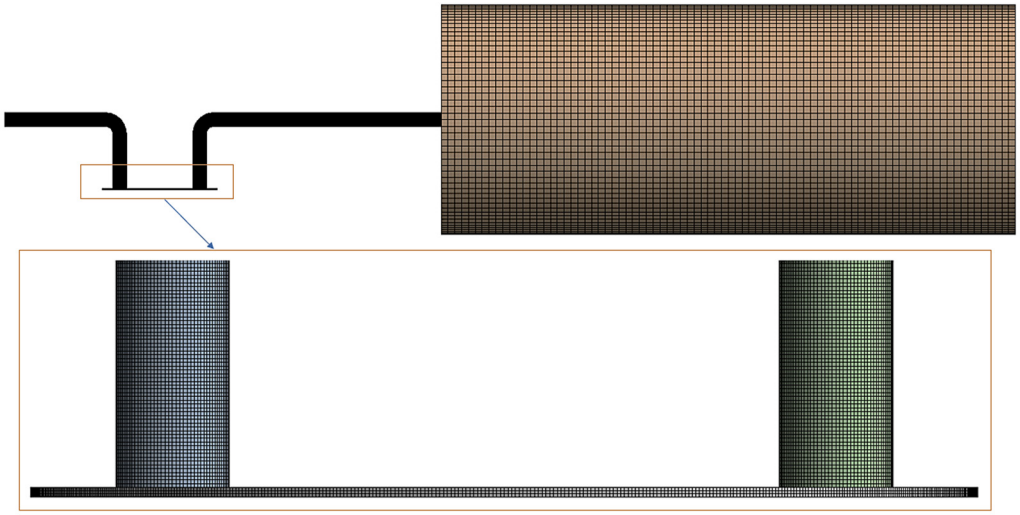


Figure 8. Mesh pattern of the computational domain.

3. Experimental Results and Analysis

3.1. Monitoring Points

To gain a deeper understanding of the operational characteristics and status of the piston-type air compressor, specific monitoring points were established on the top and bottom surfaces of the cylinder for detailed observation and analysis. The selection of monitoring points was based on the characteristics of the internal pressure distribution within the cylinder, aiming to comprehensively and accurately capture the core data of internal dynamic changes. Specifically, the monitoring points were arranged according to the positions shown in Figure 9, evenly distributed along the horizontal symmetric lines on the top and bottom surfaces of the cylinder, with 10 mm between adjacent points.

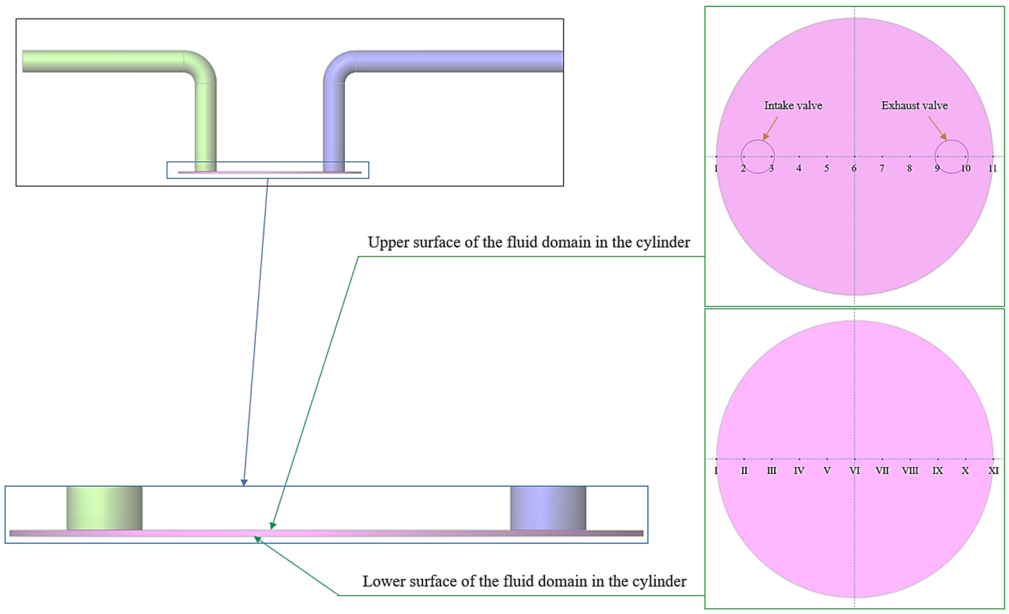


Figure 9. Schematic diagram of monitoring point positions.

Figure 10 provides a detailed illustration of the pressure variation curves at the monitoring points on the top surface of the cylinder. Through these curves, one can gain deep insights into the dynamic pressure characteristics of each monitoring point at different stages. During the intake stage, that is, before 0.0009 s, all monitoring points exhibit a consistent trend in pressure changes, characterized by a rapid decline. This

phenomenon reflects the swift drop in pressure within the cylinder during the early intake phase, possibly due to the rapid entry of air into the cylinder. Following this initial phase, the rate of pressure decrease at monitoring points 2, 3, 7, and 8 slows down compared to other points, which may be related to their specific positions inside the cylinder, leading to slightly different perceived pressure changes.

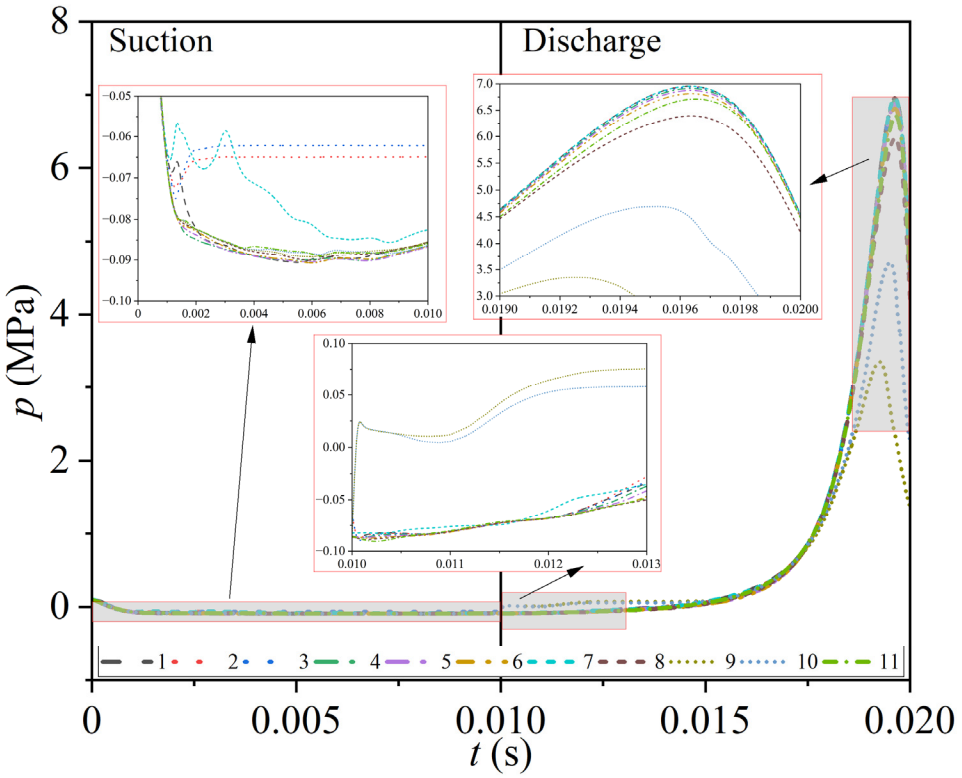


Figure 10. Pressure variation curves of monitoring points on the top surface of the cylinder.

The pressure at monitoring point 7 begins to gradually rise starting at 0.0011 s, then starts to decrease at 0.00135 s, rises again until it reaches a peak at 0.0023 s, and then begins to decrease once more to 0.003 s. Throughout this process, it shows a clear difference from the other curves. This complex pattern of pressure changes indicates that monitoring point 7 occupies a special position within the fluid dynamics environment inside the cylinder. At 0.00865 s, the trend in pressure changes at monitoring point 7 becomes like that of the remaining monitoring points (points 1, 4, 5, 6, 8, 9, 10, and 11), indicating that after this point, the pressure dynamics at monitoring point 7 tend to align with those of the other monitoring points.

The pressure at monitoring point 8 begins to rise at 0.00115 s and starts to decrease at 0.00135 s. By 0.002 s, the pressure approaches the levels observed at the other monitoring points (points 1, 4, 5, 6, 9, 10, and 11), and by 0.0023 s, the trend in pressure changes tends to align with that of the other monitoring points (points 1, 4, 5, 6, 9, 10, and 11). The pressure change pattern at monitoring point 8 shows significant variations before 0.002 s, which may be related to its specific position within the cylinder, causing it to exhibit distinct pressure dynamics during the early stage of the intake phase.

The pressure trends at monitoring points 2 and 3 are similar. Both begin to rise rapidly at 0.0013 s and gradually stabilize by 0.00285 s. The pressure at monitoring point 2 stabilizes around −0.06499 MPa, while at monitoring point 3 it stabilizes around −0.06218 MPa.

In summary, during the intake phase, the pressure changes at monitoring points 2 and 3 follow a consistent pattern: they first experience a rapid decrease, followed by a quick rise, and then a gradual increase until reaching a stable state. After 0.0035 s, the

pressure values at monitoring points 2 and 3 are relatively higher, with monitoring point 3 exhibiting a higher pressure value. This suggests that these two monitoring points may have experienced higher pressures during the later stages of the intake phase.

The pressure changes at monitoring point 7 are more complex, experiencing three decreases and two increases, with significant fluctuations in the overall curve. The pressure at monitoring point 8 shows notable changes before 0.002 s. Therefore, during the intake phase, particular attention should be paid to the material strength at the locations of monitoring points 2, 3, and 7, especially the location of monitoring point 7, where fluctuations are particularly complex. This is to ensure the safety and stability of these areas under high pressure.

During the early stage of the compression phase, due to the closure of the intake valve, the pressure at monitoring points 2 and 3 rapidly drops to −0.086 MPa before 0.0101 s, reflecting a quick decrease in internal cylinder pressure following the closure of the intake valve. Meanwhile, due to the opening of the exhaust valve, the pressure at monitoring points 9 and 10 quickly rises to 0.0212 MPa before 0.0101 s, then begins to decrease, and subsequently starts to rise again after 0.01095 s. This indicates that the opening of the exhaust valve significantly affects these monitoring points. Additionally, the pressure change patterns at the other monitoring points are relatively consistent, showing an overall gradual increase with changes within a similar range. This may reflect the similar positions of these monitoring points within the cylinder, leading to their similar pressure change patterns.

During the time interval from 0.013 s to 0.019 s, the pressure at all monitoring points generally exhibits an upward trend, with the rate of increase accelerating over time. The pressure at monitoring point 9 rises to a peak of 3.3574 MPa at 0.0192 s and then begins to decrease; the pressure at monitoring point 10 reaches its peak of 4.69139 MPa at 0.0195 s before starting to decline; the pressure at monitoring point 8 peaks at 6.40205 MPa at 0.01965 s and subsequently decreases; the pressures at the remaining monitoring points are relatively close, reaching between 6.7233 MPa and 6.9597 MPa by 0.01965 s. Based on the above data, the peak pressures at each monitoring point, arranged in ascending order, are as follows: monitoring points 9, 10, 8, 11, 6, 5, 4, 3, 2, 1, and 7, with the peak pressures at monitoring points 1 and 7 being particularly close, approximately 6.9597 MPa.

In summary, during the intake phase, monitoring points 2, 3, and 7 exhibit significant pressure fluctuations, especially at monitoring point 7, where the pressure changes are particularly complex. During the compression phase, the pressures at monitoring points 9, 10, and 8 reach higher peak values, which may be related to their positions within the cylinder and their roles during the compression process. Therefore, these specific monitoring points should be considered key areas of focus for further study to explore the internal pressure change patterns of the cylinder and their impact on overall performance.

In Figure 11, the pressure change curves of the monitoring points on the bottom surface of the cylinder are detailed, allowing for a deeper understanding of the dynamic characteristics of each monitoring point at different time intervals. During the intake phase, which occurs before 0.001 s, all monitoring points exhibit a consistent pressure change pattern characterized by a decrease in pressure values at a relatively fast rate. This phenomenon indicates that during the early stage of intake, the internal pressure of the cylinder decreases rapidly, possibly due to the quick influx of air into the cylinder.

Subsequently, the rate of pressure decrease at monitoring points II, III, VII, and VIII noticeably slows down compared to other points, and by 0.0011 s, they begin to show an upward trend. These points experience a complete cycle of rising–falling–rising–falling, eventually aligning their pressure values with those of other monitoring points. Notably,

during its first rise, monitoring point VII reaches a significant peak with a pressure value of approximately −0.04808 MPa, reflecting its special position or role in fluid dynamics.

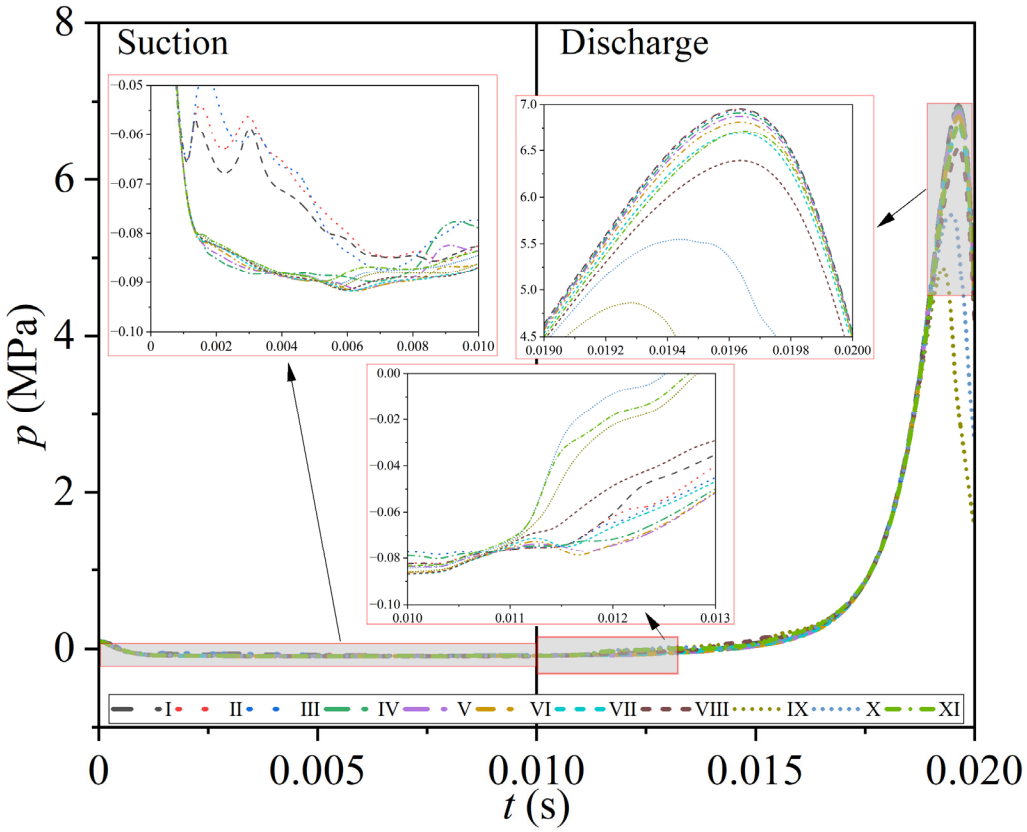


Figure 11. Pressure variation curves of monitoring points on the bottom surface of the cylinder.

In the early stage of the compression phase, up to 0.011 s, the pressure levels at all monitoring points remain relatively stable, hovering around −0.08 MPa, indicating a relatively balanced state of internal cylinder pressure. However, as the compression process progresses, the pressure change trends among monitoring points become distinctly divergent. The pressure levels at monitoring points IX, X, and XI increase rapidly, with point X exhibiting both the fastest rate of increase and the highest-pressure value, suggesting it may be a critical location during the compression process. In contrast, the pressure increase at monitoring points I and VIII is relatively slow, possibly due to their positions within the cylinder, leading to more moderate pressure changes. Meanwhile, the remaining monitoring points experience a process of initial decline followed by a rise, with this decline lasting approximately 0.00035 s, indicating that these areas may have undergone some degree of local pressure release or adjustment during this brief period.

From 0.013 s to 0.0192 s, the pressure levels at all monitoring points generally show an upward trend, with the rate of increase accelerating over time, reflecting a significant accumulation of internal cylinder pressure during the later stages of the compression process. Specifically, monitoring point IX records a pressure value of 4.8748 MPa at 0.0193 s; point X reaches 5.5641 MPa at 0.01945 s; and point VIII rises to 6.4021 MPa at 0.01965 s. The pressure values at the remaining monitoring points reach their respective peaks by 0.0196 s, ranging from 6.7 MPa to 6.96 MPa. Based on the above data, the peak pressures at each monitoring point, arranged in ascending order, are points IX, X, VIII, XI, VII, VI, V, IV, III, II and I. This differentiated pressure distribution pattern is significant for understanding the fluid dynamics mechanisms within the cylinder.

In summary, monitoring points II, III, VII, and VIII exhibit significant pressure fluctuations during the intake phase, indicating that these points may be subject to special airflow effects during the intake process. During the compression phase, points III, II, and I achieve higher pressure values, which may be related to their positions within the cylinder structure and their roles during the compression process. Therefore, these specific monitoring points should be considered key areas of focus for further study to explore the internal pressure change patterns of the cylinder and their impact on overall performance.

3.2. Lines

As illustrated in the figure, five line segments are distributed within the cylinder computational domain. They are all perpendicular to the top and bottom surfaces of the cylinder and parallel to the side walls, with each line's starting point being 35 mm away from the center point of the upper top surface of the cylinder. To gain a more comprehensive understanding of the characteristics and variation patterns of the internal flow field of the cylinder, five lines have been set up within the cylinder's computational domain. These lines are precisely positioned as labeled in Figure 12, where Line 1 is directly below the intake valve and Line 3 is directly below the exhaust valve.

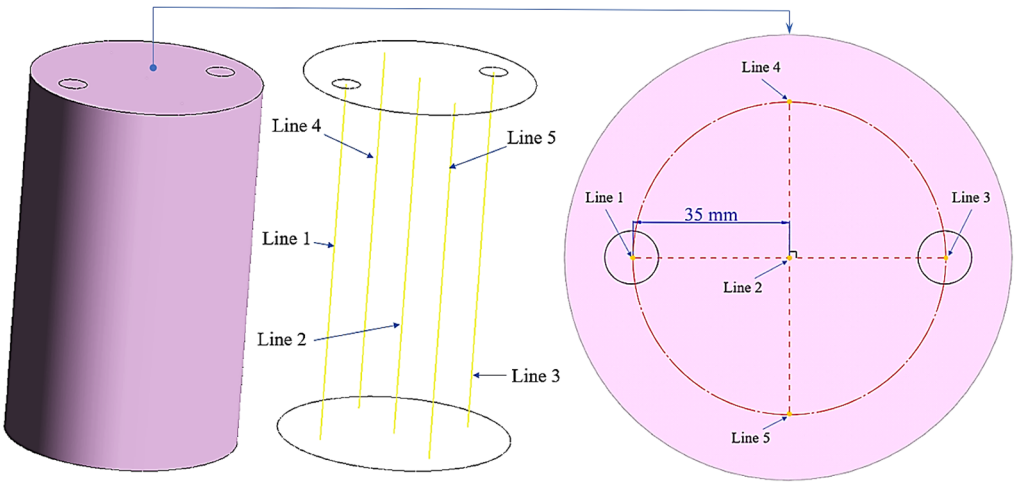


Figure 12. Schematic diagram of line positions.

All lines are oriented perpendicularly relative to the cylinder's top and bottom surfaces and parallel to its side walls, ensuring that detailed information on the internal flow can be captured from multiple angles and layers. The position of the top surface is denoted as z = 0 mm. This layout design not only takes into account the characteristics of fluid dynamics inside the cylinder but also ensures the comparability and systematic nature of the monitoring data, with the aim of providing accurate and reliable data support for subsequent analysis. Through this approach, one can achieve a more intuitive and comprehensive understanding of the operational status inside the cylinder, providing a scientific basis for optimizing cylinder performance.

Figure 13 illustrates the pressure variation curves along five lines at different time points. According to Figure 13a, at t = 0.0025 s, the pressure changes on Line 1 are particularly pronounced, mainly due to its location directly below the intake valve, exposing it to direct pressure fluctuations caused by the intake process. Specifically, at z = 0 mm, a pressure of about −57.56 kPa is recorded on Line 1, which then sharply drops to approximately −97.52 kPa within the range from z = 0 mm to z = 13.23 mm before quickly rebounding. By the end of Line 1 at this time point (z = 24.84 mm), the pressure recovers to around −53.00 kPa. In contrast, at the same time point, the pressure variations on Lines 2, 3, 4, and 5 are relatively small. The pressures on these lines remain relatively stable: around

−84.8 kPa on Line 2, about −84.1 kPa on Line 3, and roughly −85.4 kPa on Lines 4 and 5. The pressure curves for Lines 4 and 5 almost completely overlap due to their symmetrical arrangement relative to the axisymmetric plane of the computational domain, indicating that the regions where Lines 2, 3, 4, and 5 are located are relatively less affected by the intake process.

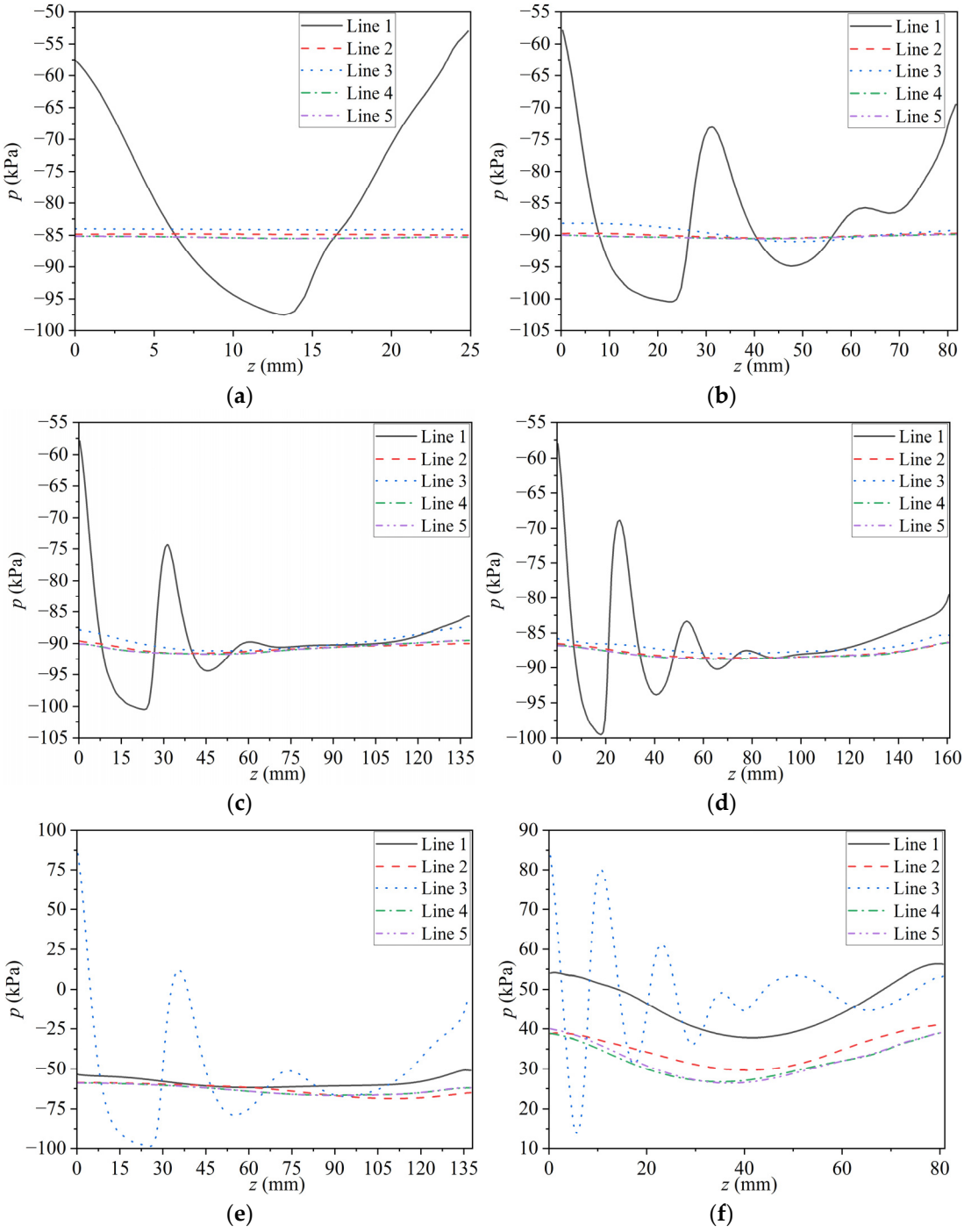


Figure 13. *Cont.*

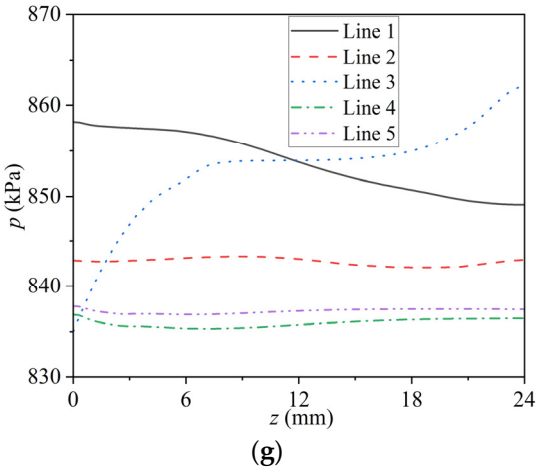


Figure 13. Pressure variation curves of five lines at multiple time points: (**a**) t = 0.0025 s; (**b**) t = 0.005 s; (**c**) t = 0.0075 s; (**d**) t = 0.01 s; (**e**) t = 0.0125 s; (**f**) t = 0.015 s; and (**g**) t = 0.0175 s.

Figure 13b shows that at t = 0.005 s, the pressure changes on Line 1 exhibit more intense fluctuations, experiencing three distinct drops and rises. These pressure troughs occur at z = 22.59 mm, 48.07 mm, and 68.40 mm, with values of −100.40 kPa, −94.84 kPa, and −86.57 kPa, respectively, while pressure peaks appear at z = 0 mm, 30.97 mm, 62.91 mm, and 81.95 mm, with values of −57.90 kPa, −73.09 kPa, −85.76 kPa, and −69.52 kPa, respectively. On Line 3, although less pronounced than on Line 1, one clear drop and one rise in pressure can still be observed: from −88.12 kPa at z = 0 mm to −91.00 kPa at z = 49.69 mm, then rising again to −89.24 kPa at z = 81.63 mm. The pressure variation trends on Lines 2, 4, and 5 are relatively consistent and minor, with overall pressure levels maintained around −90 kPa. This further confirms that these areas are less impacted by the intake process.

Figure 13c reveals that at t = 0.0075 s, the pressure on Line 1 undergoes drastic changes within the range from z = 0 mm to 70 mm. Specifically, it drops from −57.90 kPa at z = 0 mm to −100.48 kPa at z = 23.23 mm, then rises to −74.35 kPa at z = 31.30 mm, decreases again to −94.39 kPa at z = 45.82 mm, and finally rises to −89.75 kPa at z = 60.66 mm. After this point, the trend becomes smoother, slowly increasing from −89.75 kPa at z = 107.44 mm to −85.69 kPa at z = 138.09 mm. The pressure changes on Line 3 are relatively mild but show some fluctuation within the range of −91.18 kPa to −87.5 kPa. The pressure variation trends on Lines 2, 4, and 5 are similar, with small overall changes and pressure levels fluctuating between approximately −91.6 kPa and −89.48 kPa.

Figure 13d presents the situation at t = 0.01 s, where the pressure changes on Line 1 remain significant, with pressure oscillating between −57.99 kPa and −99.46 kPa, reflecting the strong influence of the intake process at this position. At this moment, Line 1 reaches peak pressures at z = 0 mm, 25.82 mm, 53.24 mm, 77.76 mm, and 161 mm, with respective values of −57.99 kPa, −68.84 kPa, −83.35 kPa, −87.51 kPa, and −79.40 kPa, while troughs are observed at z = 18.39 mm, 40.65 mm, 65.82 mm, and 89.05 mm, with respective values of −99.46 kPa, −93.83 kPa, −90.20 kPa, and −88.62 kPa. Pressure changes on other lines remain relatively mild, maintaining an overall level of around −86 kPa, further demonstrating the limited impact of the intake process on regions farther away from the intake valve.

Figure 13e indicates that at t = 0.0125 s, the pressure changes on Line 3 become exceptionally dramatic, with pressures peaking at z = 0 mm, 35.17 mm, 73.86 mm, and 137.12 mm, with respective values of −85.27 kPa, 11.60 kPa, −51.30 kPa, and −4.22 kPa; and troughs occurring at z = 24.20 mm, 54.85 mm, and 95.50 mm, with respective values of −98.32 kPa, −78.93 kPa, and −66.66 kPa. This phenomenon may be associated with adjustments in airflow direction, leading to local pressure redistribution. Meanwhile, the pressure on

Line 1 is generally higher, ranging from −62.13 kPa to −51.00 kPa, whereas the pressures on Lines 2, 4, and 5 are lower, with closer ranges between −68.7 kPa and −58.1 kPa.

Figure 13f shows that at t = 0.015 s, the pressure changes on Line 3 remain significant, experiencing five drops and five rises in pressure. Particularly in the region before z = 30 mm, the fluctuations in pressure are especially large. The maximum pressure of 83.58 kPa occurs at z = 0 mm, while the minimum pressure of 14.13 kPa is observed at z = 5.48 mm. For the other lines, the pressure change curves exhibit a concave shape, initially dropping and then rising. Specifically, Line 1 records its lowest pressure value of 37.78 kPa at z = 41.62 mm and its highest pressure value of 56.34 kPa at z = 79.69 mm. The pressure variations on Lines 2, 4, and 5 range between 26.41 kPa and 41.05 kPa.

Finally, Figure 13g points out that at t = 0.0175 s, the pressures on all five lines reach extremely high levels, ranging between 835 kPa and 863 kPa. Notably, the pressure changes on Line 3 are the most intense, especially at z = 0 mm, where the pressure is lowest at 835.04 kPa. This may be due to its location directly below the exhaust valve outlet, where increased air velocity leads to relatively lower pressure. On Line 1, the pressure is generally higher, gradually decreasing from 858 kPa to 849 kPa along the line, while the pressure changes on Lines 2, 4, and 5 are smaller. Line 2 has the highest average pressure of about 843 kPa, followed by Line 5 with an average pressure of about 837 kPa, and Line 4 has the lowest average pressure of about 835 kPa. These results indicate that during the later stages of compression, pressures in various regions gradually stabilize.

In summary, it can be concluded that during the intake process, the pressure changes on Line 1, located directly below the intake valve, are the most intense. During the compression process, the pressure changes on Line 3, located directly below the exhaust valve outlet, are also notably significant. These findings are important for understanding the characteristics of pressure distribution and their evolution over time in fluid dynamics processes.

3.3. Monitoring Surface

Figure 14 shows the variation curve of the average surface pressure and the maximum pressure on the surface of the inlet valve with time. It is observed that the trends in the variation of average pressure and maximum pressure exhibit a high degree of consistency, revealing a close relationship between these two parameters. During the initial stage of the intake phase, as the intake valve opens and the volume of the air chamber rapidly increases, the air velocity at the intake valve noticeably rises, leading to a brief drop in pressure in this region. This process continues until approximately 0.0011 s, after which the curves gradually stabilize, indicating that for most of the intake process, the pressure on the intake valve surface can remain relatively constant. This phenomenon can be attributed to the dynamic equilibrium between the change in air chamber volume and airflow.

After entering the compression phase, the average pressure undergoes a rapid negative change, dropping from an initial value of −0.06053 MPa to −0.09361 MPa. Concurrently, the maximum pressure also decreases from −0.05656 MPa to −0.08996 MPa, marking the start of the air compression process. Following this, the average pressure begins to recover at a slower rate. By 0.0131 s, the rate of pressure increase significantly accelerates, reaching a peak of 6.89573 MPa by 0.0197 s. The maximum pressure reaches its peak of 6.9455 MPa slightly earlier, at 0.0196 s. These changes reflect that the internal air compression rate within the air chamber is significantly higher than the rate at which air is expelled through the exhaust valve, resulting in a rapid accumulation of pressure within the chamber. However, when the high-pressure air inside the chamber starts to flow out through the exhaust valve in large quantities, the pressure inside the chamber quickly drops, ending

the compression process with the average pressure at 4.542536 MPa and the maximum pressure at 4.545038 MPa.

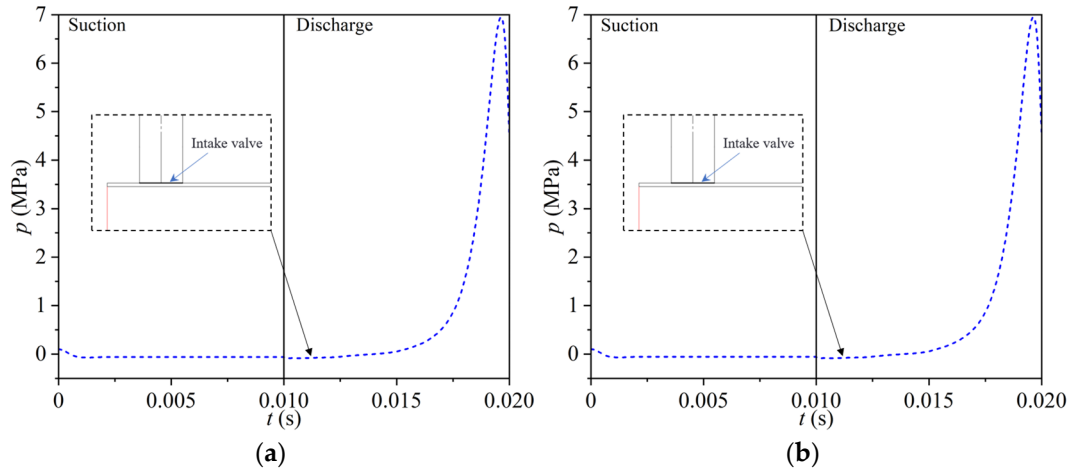


Figure 14. Pressure change curve on the intake valve surface. (**a**) Average surface pressure; (**b**) maximum pressure.

In summary, the pressure change characteristics on the intake valve surface during the intake and compression phases reveal the complex relationship between airflow and pressure changes within the air chamber. Notably, both during the intake and compression processes, the difference between the maximum pressure and the average pressure on the intake valve surface is minimal, suggesting that under the conditions of this study, the pressure distribution across different points on the valve surface is relatively uniform.

Figure 15 reveals the trends in the time evolution of average surface pressure and maximum pressure on the compressor valve surface. The data show that the pattern of pressure changes on the compressor valve exhibits a significant consistency with the pressure characteristics observed on the intake valve surface. At the initial moment of the intake phase, the pressure on the compressor valve surface rapidly increases within an extremely short period (0.00005 s). This phenomenon is fundamentally due to the direct influence of the pressure difference between the interior of the compressor piping and the air chamber on the compressor valve surface. As the internal pressure of the air chamber decreases, the pressure differential between the two areas increases, which prompts a sharp rise in pressure on the compressor valve surface. Following this, as the internal pressure of the air chamber gradually reaches a new equilibrium state, the rate of pressure change slows down until it stabilizes by the end of the intake phase.

In the early stages of the compression process, as the compressor valve opens, the air inside the compressor piping quickly moves towards the lower-pressure region of the air chamber. This process causes a significant increase in air velocity, leading to a rapid decrease in pressure on the compressor valve surface. Specifically, the average surface pressure drops from approximately 0.4 MPa to about 0.019 MPa at 0.0106 s; simultaneously, the maximum pressure also falls sharply from nearly 0.4 MPa to around 0.03187 MPa at 0.0109 s. This stage of rapid pressure drop reflects the dynamic characteristics of air rapidly transferring from a high-pressure area to a low-pressure area.

Subsequently, as the air chamber is compressed, the pressure begins to slowly recover. By 0.01525 s, both the average surface pressure and the maximum pressure exhibit a sharp upward trend, reaching peak values of 4.1623 MPa and 5.86656 MPa at 0.0195 s and 0.0196 s, respectively. After this peak, the pressures revert back and ultimately settle at approximately 2.1937 MPa for the average surface pressure and 3.79676 MPa for the maximum pressure. This behavior demonstrates the dynamic characteristics of the air dynamics

during the compression process, including the initial rapid pressure drop followed by a sharp recovery and eventual stabilization.

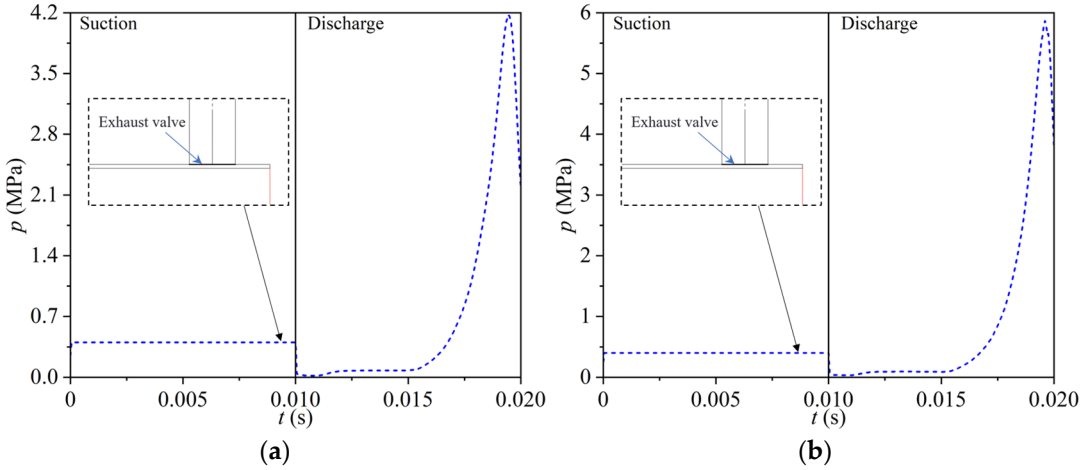


Figure 15. Pressure change curve on the compressor valve surface. (**a**) Average surface pressure; (**b**) maximum pressure.

Figure 16 illustrates the dynamic characteristics of the average surface pressure and maximum pressure on the cylinder head surface (excluding the intake valve face and exhaust valve face) over time. The research results show that in the initial stage, due to the rapid increase in the air chamber volume, the average surface pressure quickly drops from 0.0963 MPa, reaching approximately −0.0759 MPa at 0.0012 s; simultaneously, the maximum pressure also rapidly decreases from 0.1013 MPa to around −0.06651 MPa by 0.0013 s. Following this, the pressure changes gradually stabilize, maintaining a level of approximately −0.09 MPa.

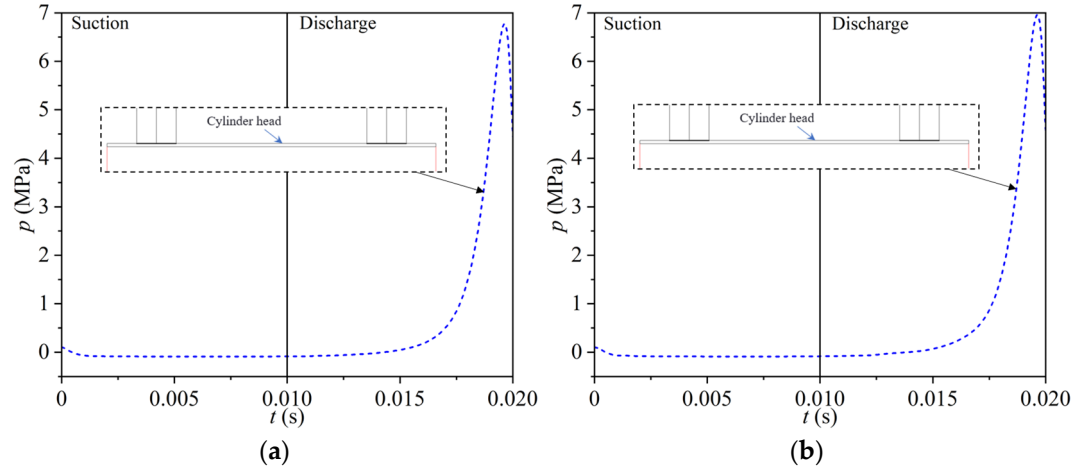


Figure 16. Pressure change curve on the cylinder head surface. (**a**) Average surface pressure; (**b**) maximum pressure.

Further analysis indicates that at the beginning of the compression phase, there is no significant change in pressure on the cylinder head surface. However, as the cylinder volume gradually decreases, the pressure starts to slowly rise. This trend continues until 0.01425 s, when the rate of pressure increase becomes notably faster. Ultimately, at 0.0196 s, the average surface pressure reaches 6.76123 MPa, while the maximum pressure rises to 6.95142 MPa. After this point, the air inside the chamber rapidly flows out at a rate exceeding the compression rate of the chamber, causing the pressure to decrease. The

average surface pressure eventually lowers to 4.44514 MPa, and the maximum pressure drops to 4.54712 MPa. These findings provide important theoretical evidence for understanding the patterns of internal pressure changes within the cylinder and their impact on engine performance.

Figure 17 shows the trend of how the average pressure and maximum pressure on the cylinder side wall surface change over time. The research findings indicate that at the beginning of the intake stroke, the pressure on the cylinder side wall exhibits a gradual downward trend. Specifically, from the experimental data, it can be observed that by 0.00105 s, the average surface pressure decreases to approximately −0.06965 MPa, while the maximum surface pressure reaches around −0.06533 MPa at 0.00115 s. Thereafter, the pressure on the cylinder side wall tends to stabilize, maintaining a level of about −0.09 MPa. Upon entering the compression stroke, this pressure value does not show significant fluctuations. However, as the compression process further develops, the pressure on the cylinder side wall begins to rise slowly. Notably, at 0.01335 s, there is a significant acceleration in the rate of pressure increase, which continues until 0.01965 s, when the average surface pressure reaches 6.84275 MPa and the maximum pressure rises to 6.9514 MPa. Finally, by the end of the experimental cycle, the average surface pressure drops to 4.49687 MPa, with the maximum pressure being 4.547116 MPa. These results reveal the complexity of the dynamic changes in internal cylinder pressure and its close relationship with the intake and compression processes.

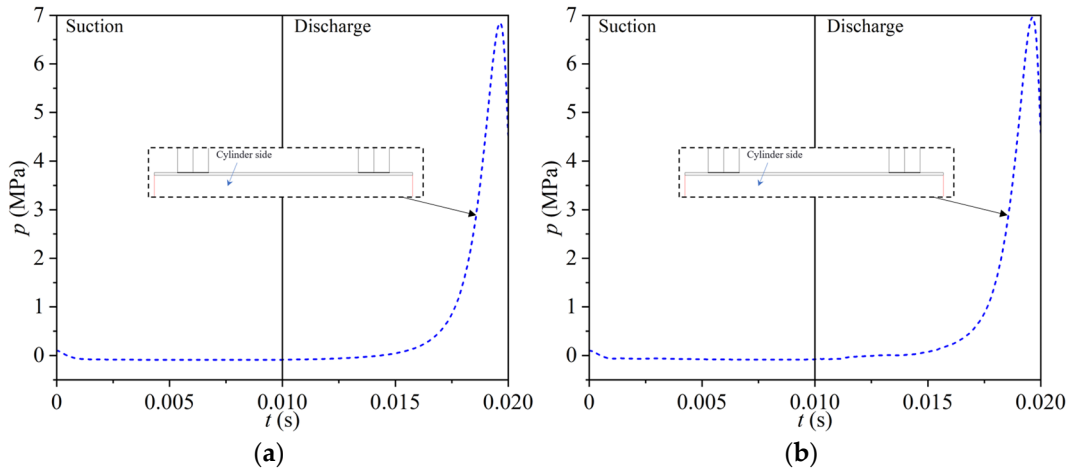


Figure 17. Pressure change curve on the cylinder side surface. (**a**) Average surface pressure; (**b**) maximum pressure.

Figure 18 shows the trend of the average pressure and maximum pressure on the bottom surface of the cylinder over time. The results indicate that during the initial stage of the intake stroke, the pressure at the bottom of the cylinder gradually decreases until it reaches a steady trend at 0.0012 s. After this point, throughout the entire intake process, the pressure at the bottom of the cylinder remains relatively stable, approximately at −0.088 MPa. As the compression stroke begins, the pressure at the bottom of the cylinder starts to rise slowly, continuing this trend up to around 0.01375 s. Following this moment, the rate of pressure increase becomes notably faster, reaching its peak by 0.0196 s, where the average surface pressure at the bottom of the cylinder reaches its highest value of 6.7500 MPa, and the maximum pressure hits 6.9510 MPa. Eventually, the average surface pressure and the maximum pressure stabilize at 4.4192 MPa and 4.5471 MPa, respectively. These data not only reflect the dynamic characteristics of pressure changes within the cylinder but also provide significant reference for further analyzing the fluid dynamics behavior during the operation of the cylinder.

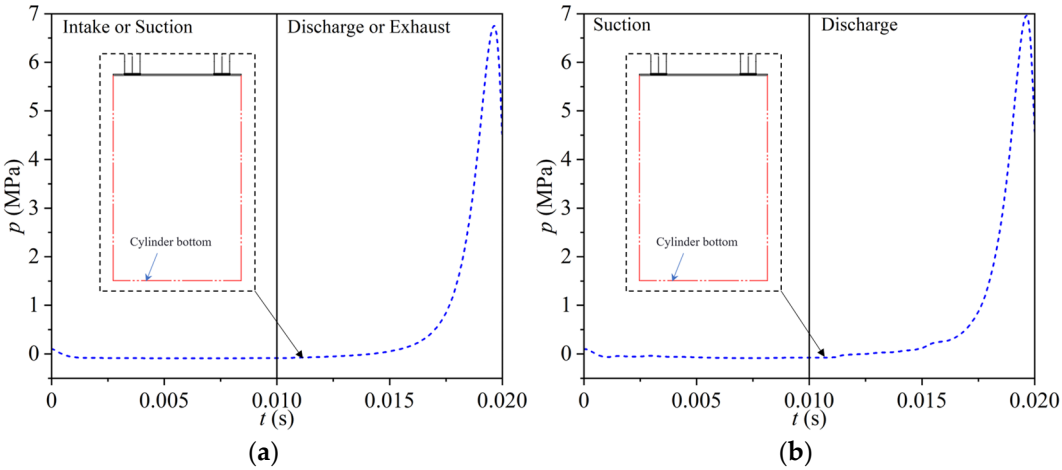


Figure 18. Pressure change curve on the cylinder bottom surface. (**a**) Average surface pressure; (**b**) maximum pressure.

3.4. Monitoring Body

Targeting the volumetric average pressure changes within each component of the computational domain, a detailed description is provided, with the results shown in Figure 19. During the initial stage of the intake phase, due to the rapid increase in cylinder volume, it prompts the air in the intake manifold to quickly pass through the intake valve into the cylinder, leading to a significant decrease in the average pressure inside the intake manifold and the cylinder (see Figure 19a,c). Experimental data show that before 0.001 s, the average pressure inside the intake manifold rapidly drops to −0.03702 MPa; at 0.001 s, the average pressure inside the cylinder decreases to −0.06717 MPa, after which it tends to stabilize. Subsequently, at 0.00145 s, the average pressure inside the intake manifold recovers to −0.03420 MPa and gradually reaches a stable state. This phenomenon is attributed to the formation of a relatively stable balance between the rate of air inhalation and the expansion rate of the air chamber volume. It is worth noting that because the exhaust valve remains closed during this phase, the average pressure inside the exhaust manifold and the air storage tank does not change throughout the entire intake process.

During the pressure variation process, as shown in Figure 19a, after the intake valve closes, the average pressure inside the intake manifold exhibits a fluctuating characteristic, with the amplitude of fluctuations gradually decreasing over time until it ultimately tends toward 0 MPa. The change in volumetric average pressure inside the cylinder (see Figure 19c) is largely consistent with the pressure change trends on the top, side, and bottom surfaces of the cylinder. Specifically, at 0.014 s, the average pressure inside the cylinder begins to slowly rise, then rapidly increases to 6.7459 MPa at 0.01965 s, and finally decreases to approximately 4.417722 MPa. For the compression process, as shown in Figure 19b, in its early stage, because the initial pressure inside the exhaust manifold is higher than that inside the air chamber, air rapidly flows from the exhaust manifold into the air chamber, causing the pressure inside the exhaust manifold to rapidly drop to 0.182259 MPa by 0.0114 s. Following this, the pressure changes inside the exhaust manifold are relatively mild until 0.0159 s, when, with the increase in cylinder pressure, air starts to flow back rapidly from the cylinder into the exhaust manifold, resulting in the pressure inside the exhaust manifold rising rapidly to 2.5099 MPa by 0.01955 s. Subsequently, because the pressure of the air inside the exhaust manifold is greater than that inside the air storage tank, air begins to flow into the air storage tank, causing the pressure inside the tank to drop to about 1.8156 MPa.

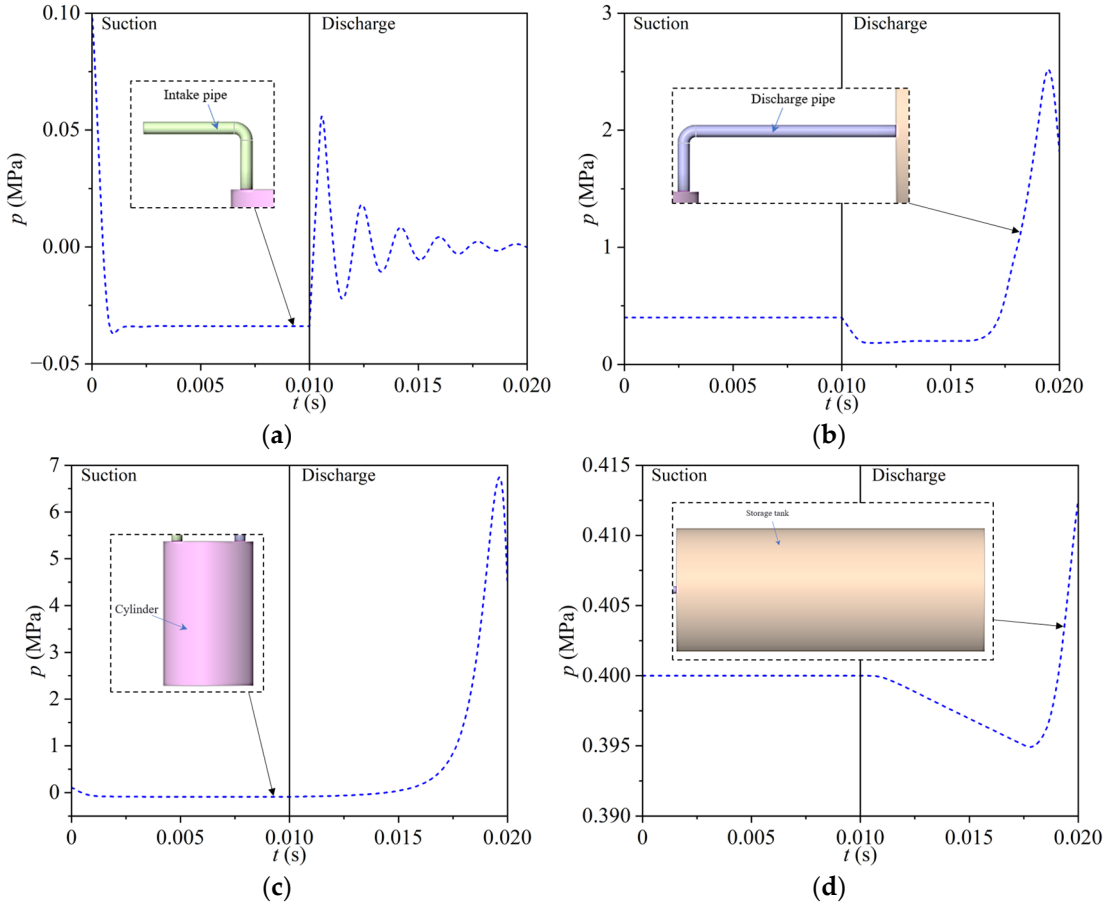


Figure 19. Average pressure change curve of the monitoring body. (**a**) Intake pipe; (**b**) discharge pipe; (**c**) cylinder; and (**d**) storage tank.

The pressure change situation inside the air storage tank (see Figure 19d) shows that it remains relatively stable for most of the compression process duration. This is because the air near the connection between the exhaust manifold and the air storage tank has not yet begun to flow rapidly. Until 0.0106 s, the air inside the air storage tank begins to flow towards the exhaust manifold until 0.0179 s, when the average pressure inside the air storage tank drops to 0.3949, at which point the airflow between the air storage tank and the exhaust manifold also reaches a relatively balanced state. Following this, air rapidly flows from the exhaust manifold into the air storage tank, causing the pressure inside the air storage tank to rise sharply.

Targeting the changes in the total mass of air within each component of the computational domain, a detailed depiction is provided, with results shown in Figure 20. In Figure 20a, the change in the total mass of air inside the intake manifold is illustrated. Initially, the mass of air decreases rapidly due to the swift increase in cylinder volume. Until 0.00095 s, the rate of decrease in air mass slows down, followed by an acceleration in the rate of decline until it stabilizes around 0.00001512 kg at approximately 0.0026 s. During the subsequent compression process, the curve of total air mass changes similarly to its pressure change curve, eventually trending towards stabilization at about 0.00001926 kg.

Figure 20c shows the variation in the total mass of air inside the cylinder. During the intake process, as expected, the total mass of air gradually increases. The trend in the mass curve can intuitively represent its mass flow rate.

Following this, during the compression process, the increase in mass is due to the backflow of air through the exhaust valve until the mass reaches 0.00087975 kg at 0.01725 s, after which the air starts to flow out through the exhaust valve gradually.

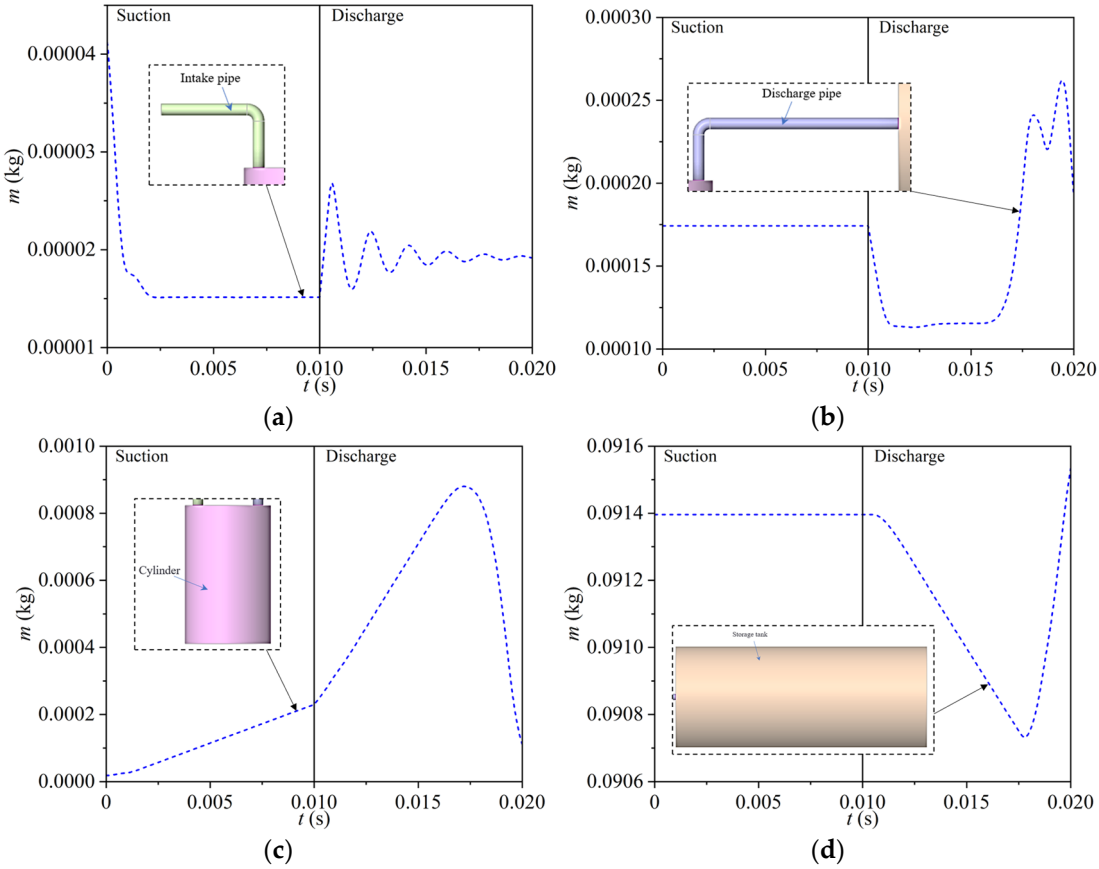


Figure 20. Mass change curve of the monitoring body. (**a**) Intake pipe; (**b**) discharge pipe; (**c**) cylinder; and (**d**) storage tank.

In Figure 20b, the change in the total mass of air inside the exhaust manifold is depicted. During the intake process, due to the closure of the intake valve, there is no significant change in the total mass of gas. At the beginning of the compression process, because air flows from the exhaust manifold into the cylinder, the total mass of air inside the exhaust manifold drops sharply until it becomes relatively stable at around 0.00011366 kg at 0.0115 s. Subsequently, at 0.0156 s, the total mass inside the exhaust manifold begins to rise quickly. This increase is due to the flow of air from the air storage tank into the exhaust manifold until 0.01805 s, when the air starts to flow from the exhaust manifold into the air storage tank. Between 0.0187 and 0.0195 s, the mass inside the exhaust manifold rises again because less air flows from the exhaust manifold into the air storage tank than flows from the cylinder into the exhaust manifold. After 0.0195 s, more air flows from the exhaust manifold into the air storage tank compared to what flows from the cylinder into the exhaust manifold, leading to a rapid decrease once more. The above results provide critical data support for gaining a deeper understanding of the operational mechanism of the compressor and internal air dynamics behavior.

3.5. Pressure Contour

To more intuitively analyze the internal flow characteristics of a piston-type air compressor during its operation, detailed analyses were conducted using contour maps that depict pressure distribution at specific local regions at eight selected time points. These contour maps are presented in Figures 21–28. The contour maps not only help reveal the precise flow state of the air at each moment but also provide crucial insights into the fluid dynamics behavior within the compressor, thereby offering scientific evidence for design optimization and performance improvement.

At time t = 0.0025 s, the contour map showing pressure distribution on the symmetry plane of the intake manifold and cylinder is illustrated in Figure 21.

The results show that two significant low-pressure areas with pressure values of approximately −92 kPa are observed in the small corner at the lower left of the intake manifold. Notably, most of the space within this particular area has a pressure around −50 kPa, indicating a notable pressure gradient change within the region. In contrast, the large corner at the upper right of the intake manifold exhibits significantly higher pressure values, about −20 kPa, further revealing the impact of different geometric structures on fluid dynamics behavior.

From an overall trend perspective, the pressure gradually decreases from the entrance of the exhaust manifold to the intake valve area, specifically decreasing from approximately −22 kPa at the entrance to about −57 kPa near the intake valve. This phenomenon reflects energy loss during the airflow process and implies the important influence of the intake valve on the airflow path and pressure distribution. Moreover, this pressure drop trend does not terminate upon reaching the intake valve but extends for a certain distance, up to about 16 mm below the valve, where the pressure begins to rise and continues to increase along the direction toward the bottom surface.

Additionally, it was found that apart from the aforementioned specific regions, most locations have not been significantly affected by external fluids, with pressures maintained at around 84 kPa. Notably, there is a marked increase in pressure in the local area of the lower-left corner of the air chamber, reaching approximately −71 kPa, while the pressure drops to a lower level, about −95 kPa, within the range of about 9 mm to 15 mm directly below the exhaust valve. When moving down beyond 15 mm, the pressure gradually recovers to a level of approximately −60 kPa. These findings indicate that below the intake valve, there is a significant change in the properties of the gas, and along the direction from the intake valve to the bottom, the pressure exhibits a nonlinear variation pattern of "high → low → high".

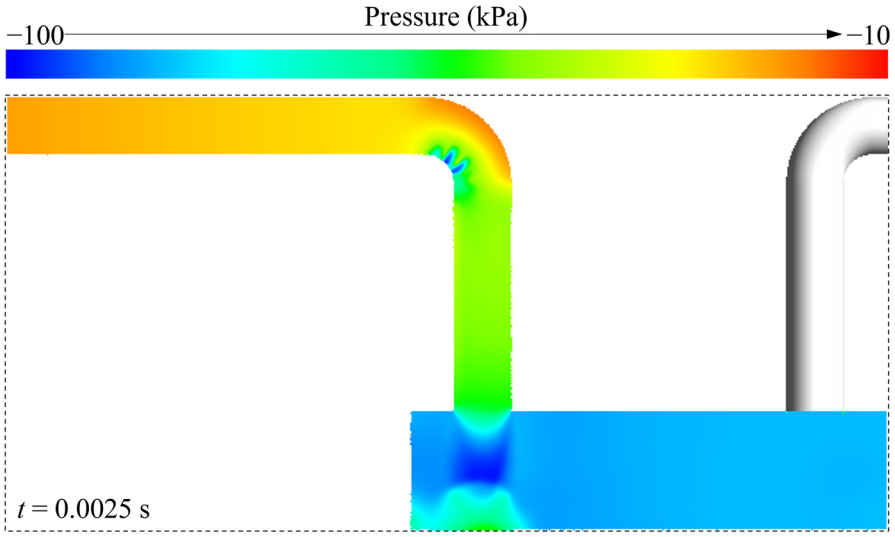


Figure 21. The velocity contour on the symmetry plane of the intake manifold and cylinder at t = 0.0025 s during the intake process.

At time t = 0.005 s, the contour map showing pressure distribution on the symmetry plane of the intake manifold and cylinder is depicted in Figure 22.

At the time point of 0.005 s, the characteristics of pressure distribution within the manifold intake are largely consistent with those at 0.0025 s, demonstrating the continuity and stability of the flow field over time. Specifically, the small corner located at the lower left of the intake manifold still maintains a relatively low-pressure level of approximately

−50 kPa, with two points of extremely low pressure close to −92 kPa within this area. In contrast, the large corner at the upper right of the intake manifold has relatively higher-pressure values around −20 kPa, highlighting the influence of different geometric structures on the internal pressure distribution of the fluid.

Throughout the interior of the intake manifold, there is a clear gradient change in pressure distribution, gradually decreasing from about −22 kPa near the intake opening to approximately −56.56 kPa at the location of the intake valve. Notably, starting from the position of the intake valve, the pressure continues to drop until it reaches approximately −95 kPa about 25 mm below the valve. Between 28 mm and 34 mm below the valve, there appears a high-pressure zone with a diameter of roughly 3 mm, where the pressure value is about −72 kPa, which may be due to changes in local flow structure. Following this, the pressure along the direction below the intake valve continues to decrease until it reaches approximately −92 kPa at 54 mm. As we move further down, the pressure gradually recovers, eventually reaching about −71.1 kPa at the bottom.

In summary, the pressure distribution within the intake manifold undergoes a nonlinear variation pattern of "high → low → high → low → high", revealing the complexity of the pressure distribution mode. This complex pattern not only illustrates the diversity of fluid dynamics behavior during the intake process but also provides important reference information for the further optimization of the intake system design.

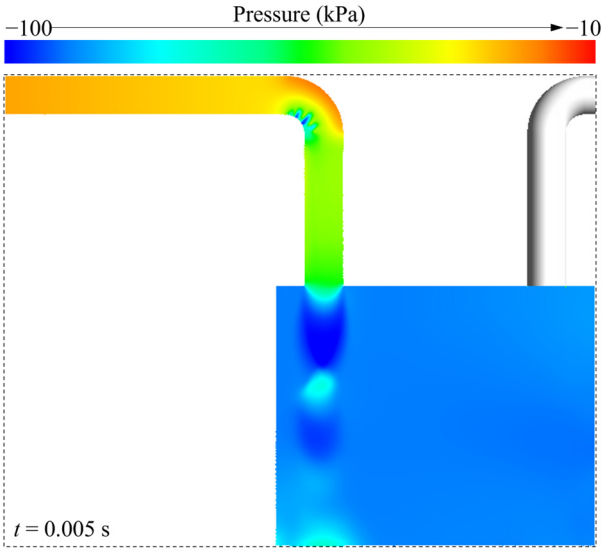


Figure 22. The velocity contour on the symmetrical plane of the intake manifold and cylinder at t = 0.005 s during the intake process.

At time t = 0.0075 s, the contour map of pressure distribution on the symmetry plane of the intake manifold and cylinder is shown in Figure 23. The results indicate that at this time point, the characteristics of pressure distribution within the intake manifold are largely consistent with those observed at previous time points (i.e., t = 0.0025 s and t = 0.005 s), reflecting the continuity and stability of the flow field as it evolves over time. Specifically, the small curved area at the lower left of the intake manifold continues to maintain a relatively low pressure level, approximately −50 kPa, with two points of extremely low pressure close to −91 kPa present within this region. In contrast, the large curved area at the upper right of the intake manifold shows higher pressure levels, around −19.5 kPa, highlighting the significant impact of different geometric structures on the internal pressure distribution of the fluid.

Further analysis of the pressure distribution throughout the entire intake manifold reveals a clear gradient change from the intake opening to the position of the intake valve,

decreasing gradually from about −22.5 kPa near the intake opening to nearly −56.62 kPa close to the intake valve. Notably, starting from below the intake valve, the pressure continues to drop along the axial direction until reaching its lowest point approximately 25 mm below the valve, where the pressure value is about −95.76 kPa. Following this, the pressure begins to gradually recover, forming a small region with a radius of about 3 mm and a pressure of approximately −75 kPa around 28 mm below the valve. Afterward, the pressure drops again, while outside of the specific regions, pressure changes are relatively minor, with the pressure from the top surface of the cylinder to the bottom surface generally maintained at around −90 kPa. This result suggests that during the intake process of the piston-type air compressor, the airflow mainly affects the pressure characteristics of a small area directly below the intake valve, with limited influence on other areas.

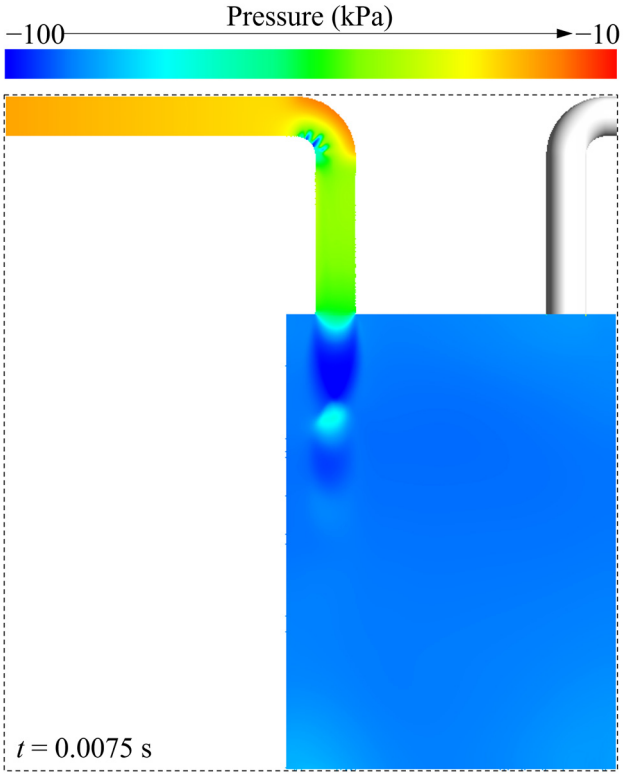


Figure 23. The velocity contour on the symmetry plane of the intake manifold and cylinder at t = 0.0075 s during the intake process.

At time t = 0.01 s, the contour map of pressure distribution on the symmetry plane of the intake manifold and cylinder is shown in Figure 24. At this moment, the intake phase of the piston-type air compressor has been completed. The characteristics of pressure distribution within the manifold intake are like those at previous moments, showing a certain continuity. Specifically, the small curved area at the lower left of the intake manifold still exhibits relatively low pressure, approximately −50 kPa, with two regions of even lower pressure around −90 kPa present within this area. In contrast, the large curved area at the upper right of the intake manifold shows higher pressure, about −20 kPa. Overall, the pressure decreases gradually from the intake opening to the intake valve, reducing from about −22 kPa to approximately −56.7 kPa.

Further observation of the pressure changes below the intake valve reveals that the pressure continues to drop until it reaches approximately −92 kPa about 21 mm below the valve. After this point, the pressure forms a region with a diameter of about 3 mm where the pressure is around −70 kPa. Subsequently, the pressure drops again, reaching another low point of −92 kPa at approximately 45 mm below the valve. Following this,

the pressure slowly rises to −84.6 kPa at 56 mm and then gradually decreases once more, reaching −89 kPa at about 70 mm.

Additionally, apart from the specific region directly below the intake valve, most areas within the cylinder maintain relatively low-pressure levels. Specifically, the pressure in the upper part of the cylinder is roughly maintained at −86.5 kPa, while in the lower part, it is approximately −85 kPa. This indicates that by the end of the intake phase, the overall pressure difference between the top and bottom of the cylinder is only around 1.5 kPa. These observations suggest that after the completion of the intake phase in a piston-type air compressor, the pressure distribution inside the cylinder exhibits a certain regularity, which is important for understanding the working principle of the compressor and optimizing its performance.

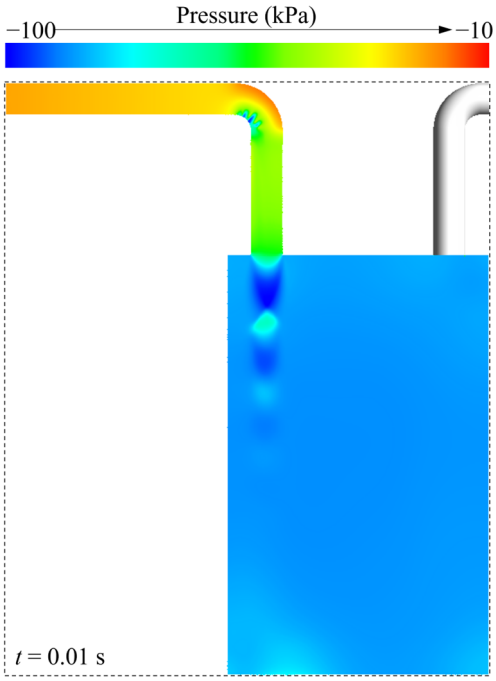


Figure 24. The velocity contour on the symmetry plane of the intake manifold and cylinder at t = 0.01 s during the intake process.

At time t = 0.0125 s, the contour map of pressure distribution on the symmetrical plane of the exhaust manifold and cylinder is depicted in Figure 25. Due to the opening of the exhaust valve and the pressure within the exhaust manifold being higher than that inside the cylinder, air exhibits a reverse flow from the exhaust manifold into the cylinder, resulting in a noticeable backflow phenomenon. The observation results show that the characteristics of the air in reverse flow still follow a nonlinear distribution pattern of "high → low → high → low → high". As the compression process progresses, the air within the cylinder is continuously compressed, driving the air to move upward from the bottom of the cylinder, thereby forming a distinct low-pressure area in the middle of the cylinder. Especially on the cross-section of the cylinder, except for the corner near the exhaust valve, the pressure in the other three corners is significantly higher than in the central region. Among these, the pressure in the lower right corner reaches around −13 kPa, while the pressure in the central region is only about −68.3 kPa. Simultaneously, it can be observed that there is also a low-pressure area in the small corner at the lower right of the exhaust manifold, indicating that this characteristic is common.

This pressure distribution feature indicates that the opening of the exhaust valve and the relatively higher pressure within the exhaust manifold are the main causes of the backflow phenomenon, and the compressive motion of the air inside the cylinder further

intensifies the low-pressure state in that central region. Additionally, the high-pressure areas in the four corners of the cylinder reflect the complexity and non-uniformity of the airflow path.

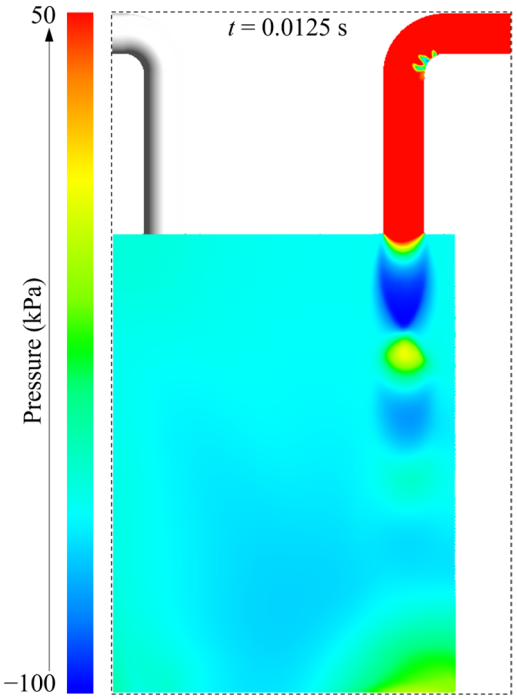


Figure 25. The velocity contour on the symmetry plane of the intake manifold and cylinder at t = 0.0125 s during the compression process.

At time t = 0.015 s, the contour map of pressure distribution on the symmetry plane of the exhaust manifold, cylinder, and part of the air storage tank is shown in Figure 26. At this moment, the small corner regions within the exhaust manifold still exhibit relatively low pressure, with several areas of extremely low pressure having values around 10 kPa, whereas the large corner regions have higher pressures, approximately 250 kPa. As the compression process continues, that is, with the compressive action of the cylinder, although the backflow phenomenon still exists, its intensity has begun to weaken. Observations show that the pressure around the cylinder is relatively high, ranging between 50 and 90 kPa, while the pressure in the central region is significantly lower, around 30 kPa. This phenomenon indicates that during the compression process, the pressure in the central region of the cylinder is notably lower than the surrounding areas, possibly due to the air diffusing outward as it is compressed within the cylinder.

These results further confirm the complexity of the pressure distribution within the exhaust manifold and cylinder, as well as the impact of the compression process on the flow pattern of air inside the cylinder. The significant difference between the lower-pressure state in the central region and the higher-pressure state in the surrounding areas of the cylinder is crucial for understanding the working mechanism of the piston-type air compressor during the compression phase and for optimizing its performance.

At time t = 0.0175 s, the contour map of pressure distribution on the symmetry plane of the exhaust manifold, cylinder, and part of the air storage tank is depicted in Figure 27. At this stage, which is late in the compression phase, observations indicate a very uniform pressure distribution. Specifically, air flows rapidly from the cylinder into the air storage tank with a notably uniform flow pattern. There are no significant differences in pressure at the various corners of the exhaust manifold, possibly due to the overall high-pressure environment. At this moment, the pressure inside the cylinder has reached approximately

850 kPa, much higher than the pressure within the air storage tank, which is around 395 kPa.

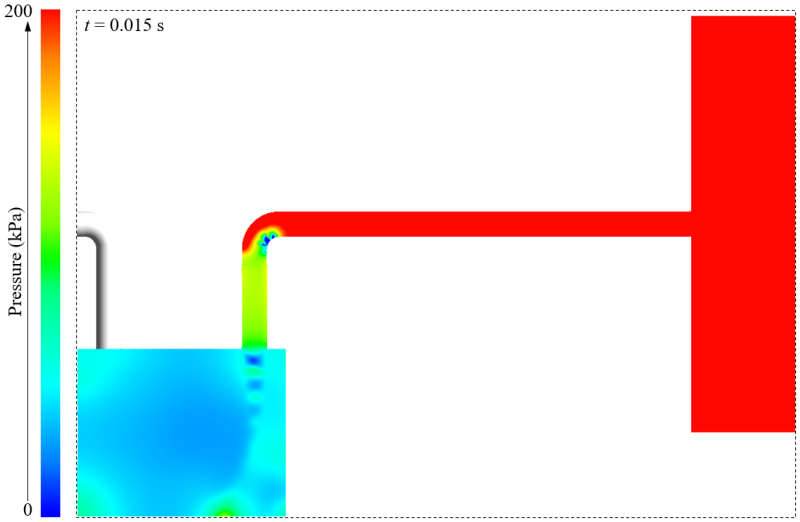


Figure 26. The velocity contour on the symmetry plane of the intake manifold and cylinder at t = 0.015 s during the compression process.

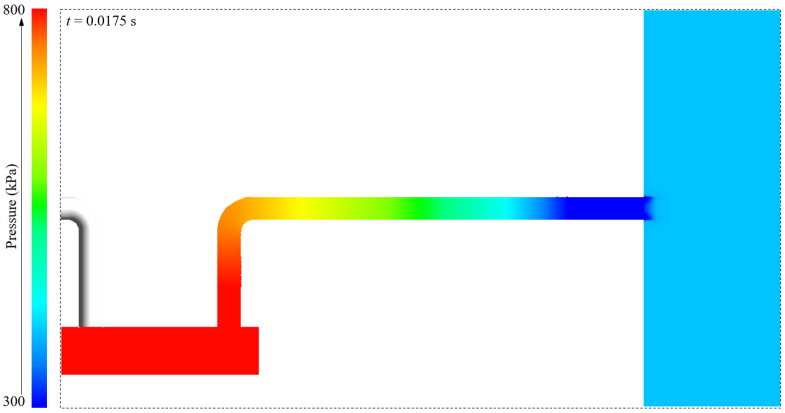


Figure 27. The velocity contour on the symmetry plane of the intake manifold and cylinder at t = 0.0175 s during the compression process.

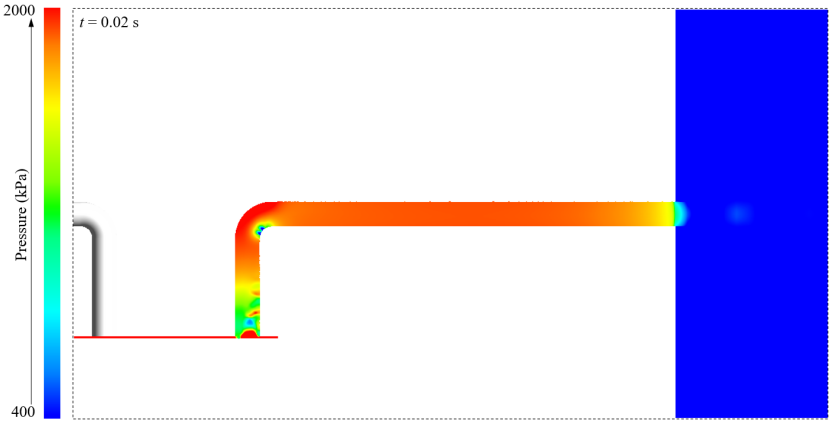


Figure 28. The velocity contour on the symmetry plane of the intake manifold and cylinder at t = 0.02 s during the compression process.

It is worth noting that the pressure near the end of the exhaust manifold closer to the air storage tank is lower, only about 248 kPa. This phenomenon could be attributed to an increase in flow velocity leading to a local pressure drop. As the high-pressure air swiftly

passes through the pipeline into the air storage tank, the rapid movement of air creates a low-pressure effect in the local areas it traverses, in accordance with Bernoulli's principle, which states that an increase in fluid velocity results in a decrease in pressure.

These observations suggest that during the later stages of the compression phase, the pressure difference between the cylinder and the air storage tank significantly increases, prompting air to flow from the cylinder to the air storage tank at a high speed, which in turn leads to a localized pressure drop within the exhaust manifold. Such a uniform pressure distribution and airflow pattern are crucial for ensuring efficient operation of the compressor and optimizing its performance.

At time t = 0.02 s, the contour map of pressure distribution on the symmetry plane of the exhaust manifold, cylinder, and part of the air storage tank is shown in Figure 28. At this point, the compression process has ended. Due to a lack of sufficient air remaining in the cylinder to continue being forced into the pipeline, the pressure distribution within the exhaust manifold is no longer uniform, and the airflow becomes somewhat chaotic. Specifically, the pressure near the exhaust valve is approximately 1200 kPa across most of the region, while in the middle section of the pipeline, the pressure significantly increases to about 1880 kPa. Notably, there is once again an appearance of low-pressure areas in the small, curved regions at the bends of the pipeline, with several relatively very low-pressure zones present, whereas the larger curved regions exhibit relatively higher pressures.

These phenomena indicate that after the completion of the compression process, the insufficient supply of air from the cylinder has led to the loss of uniformity in the airflow within the exhaust manifold, resulting in complex pressure distributions. The low pressure in the small curved regions may be associated with flow separation and reattachment of the gas, while the high pressure in the large curved regions could be due to air accumulation or flow obstruction in these areas.

3.6. Discussion

The dynamics of the valve have a significant impact on pressure pulsations within the cylinder. The valve mechanism studied in this paper employs an active control method primarily because the research focuses on the pressure field analysis of the core components (cylinder and storage tank). This approach isolates and analyzes the evolution of the pressure field caused by piston motion in the system without considering valve dynamics. Such simplification is necessary to address the pressure field response driven by piston-induced disturbances without introducing the complexity of valve motion hysteresis. It also allows for the quantification of the pressure pulsation threshold induced solely by the reciprocating flow inertia and compressibility effects.

During the periodic reciprocating motion of the piston, friction at the cylinder wall generates a continuous heat-work conversion effect, leading to gas temperature rise and heat accumulation in the piston chamber, which influences the internal pressure distribution. However, in this theoretical calculation, given the very brief duration of a single operating cycle (only 0.02 s), the limited time available for effective heat conduction between the model and the external environment has a minimal impact on internal pressure. Therefore, thermal exchange between the system and the surrounding environment is not considered in this phase.

4. Conclusions

This study carried out a detailed simulation analysis of the compression process in a piston-type air compressor using Fluent software (version 2020 R2), revealing the complexity of the internal fluid characteristics of the compressor. Especially, the research delved into the pressure changes within different monitoring points, monitoring surfaces,

and computational domains of each component inside the cylinder, providing valuable data support for understanding the fluid dynamic behavior during the operation of the compressor. The specific results are as follows:

(1) The pressure distribution inside the cylinder exhibits complex nonlinear variation patterns, especially below the intake valve, where the air characteristics change significantly, showing a "high → low → high" pressure change pattern.
(2) As the compression process progresses, particularly in the later stages of compression, the pressure difference between the cylinder and the storage tank increases significantly, promoting the rapid flow of air from the cylinder to the storage tank, leading to localized pressure drops within the discharge pipeline.
(3) After the compression process ends, insufficient air supply in the cylinder leads to non-uniform airflow within the discharge pipeline, forming a complex pressure distribution. Low-pressure areas in small curved regions may be related to flow separation and reattachment, while high-pressure areas in large curved regions could be due to air accumulation or flow obstruction in those regions.
(4) In the early stage of the intake phase, the pressure change trend at all monitoring points is consistent, characterized by a rapid decline, reflecting the quick decrease in pressure along the horizontal lines on the top and bottom surfaces of the cylinder during the initial intake period. The pressure change pattern at Monitoring Point 7 (with complex fluctuations) shows a marked difference, indicating its unique position within the cylinder's fluid dynamic environment.
(5) The pressure changes on the intake valve surface show a high degree of consistency between the average surface pressure and the maximum pressure, indicating a close relationship between the two. During the intake phase, the valve surface pressure briefly decreases before stabilizing; entering the compression phase, the pressure rapidly shifts negatively before slowly recovering and then quickly decreases again when compression ends. Notably, the small difference between the maximum and average pressures suggests a uniform pressure distribution across the valve surface. The pressure changes on the exhaust valve surface are similar to those on the intake valve.
(6) Pressure changes on Line 3 become exceptionally intense during the compression process, associated with adjustments in the direction of airflow, leading to a redistribution of pressure in local areas. This indicates that during the intake process, the pressure changes on Line 1, located directly below the intake valve, are most pronounced, while during compression, the pressure changes on Line 3, located directly below the exhaust valve, are also significant.
(7) As air flows into the storage tank, its pressure decreases but remains mostly stable until airflow reaches equilibrium, causing the storage tank pressure to rise. During intake, the mass of air inside the inlet pipe rapidly decreases before gradually stabilizing, while the mass of air inside the cylinder increases. During compression, the reverse flow increases to a maximum before decreasing as it exits the system.
(8) During the intake process, Line 1, located directly below the intake valve, is exposed to significant pressure changes caused by the intake process. At the same time point, the amplitude of pressure changes on Lines 2, 3, 4, and 5 is smaller, indicating that these lines are relatively less affected by the intake process.
(9) A notable low-pressure area was observed in the small corner below the left side of the intake pipe, while the pressure value was significantly higher in the large corner above the right side, demonstrating the flow characteristics and energy loss conditions of fluids under different geometric conditions.

Therefore, during the design phase, it is crucial to focus on improving the internal structure of the cylinder, such as introducing flow control devices to reduce pressure fluctu-

ations and ensure stable and efficient airflow. Special channel designs are needed in the area below the intake valve to mitigate pressure changes. Materials with better wear resistance should be selected for the valves, and their opening and closing mechanisms should be optimized, which not only helps reduce energy loss but also extends the equipment's lifespan. For pipeline systems, especially at bends, increasing the curvature radius and using more efficient flow guidance devices can decrease the occurrence of local low-pressure areas, thereby enhancing system efficiency.

In future work, the introduction of temperature distribution analysis, vibration analysis, and acoustic characteristics analysis will enable a more comprehensive assessment of the operating status and performance of piston-type air compressors. These methods facilitate an in-depth understanding of the complex hydrodynamic behavior within cylinders, thereby effectively monitoring the mechanical condition and potential faults during equipment operation.

Author Contributions: Conceptualization, H.-F.H.; methodology, B.-Y.Z.; software, H.-B.L.; investigation, W.-W.T.; writing—original draft preparation, Y.-J.Z.; writing—review and editing, Y.-J.W.; supervision, Y.-L.Z.; project administration, L.-H.T. All authors have read and agreed to the published version of the manuscript.

Funding: The research was financially supported by the Science and Technology Project of Quzhou (No. 2023K256, No. 2023NC08, and No. 2022K41), the Research Grants Program of the Department of Education of Zhejiang Province (No. Y202455709), teaching reform projects for vocational education in Zhejiang Province during the 14th Five-Year Plan period (No. jg20230255), and the Zhejiang Provincial Natural Science Foundation of China (No. LZY21E050001).

Data Availability Statement: The data that support the findings of this study are available from the corresponding author upon reasonable request.

Conflicts of Interest: Author Bing-Yin Zhou was employed by State Grid Corporation of China United Pipeline Co., Ltd., West East Gas Pipeline Branch. The remaining authors declare that the research was conducted in the absence of any commercial or financial relationships that could be construed as a potential conflict of interest.

Nomenclature

x	Piston displacement
v	Piston velocity
ρ	Fluid density
u, v, and w	Velocity components in the radial, circumferential (or tangential), and axial directions, respectively
p	Pressure
μ	Dynamic viscosity
F_{r}, F_{θ}, and F_{z}	Forces in the radial, circumferential, and axial directions
c_p	Specific heat capacity
T	Temperature
k	Thermal conductivity
Φ	Heat source term due to viscous dissipation
r	Ratio of mesh cell counts
N	Number of grids
e	Relative error
f	Monitored value
GCI	Grid convergence index

References

1. Shatalov, I.K.; Antinov, Y.A.; Smirnov, S.V.; Mamaev, V.K.; Ramazanov, É.R.; Shkarin, K.V. State of Gas in a Piston Compressor at the Start of Compression. *Chem. Pet. Eng.* **2019**, *54*, 835–841. [CrossRef]
2. Selvaraj, G.; Yessian, S.; Ramalingam, S.; Kumar, S.D.; Gopal, G.; Sharma, S.; Kumar, A.; Li, C.; Abbas, M. Investigation on topology-optimized compressor piston by metal additive manufacturing technique: Analytical and numeric computational modeling using finite element analysis in ANSYS. *Open Phys.* **2023**, *21*, 20220259. [CrossRef]
3. Fritz, B.; Scheichl, B. Comprehensive multi-scale cylinder lubrication model for reciprocating piston compressors: From rigid-body dynamics to lubricant-flow simulation. *Tribol. Int.* **2023**, *178*, 108028. [CrossRef]
4. Khaljani, M.; Vennard, A.; Harrison, J.; Surplus, D.; Murphy, A.; Mahmoudi, Y. Experimental and modelling analysis of efficiency enhancement in a liquid piston gas compressor using metal plate inserts for compressed air energy storage application. *J. Energy Storage* **2021**, *43*, 103240. [CrossRef]
5. Khait, A.; Shcherba, V.; Nosov, E. Numerical and experimental investigation of the hybrid piston compressor using the novel multi-time-scale OpenFOAM®-based model. *Appl. Therm. Eng.* **2024**, *249*, 123448. [CrossRef]
6. Silva, E.; Dutra, T. Piston trajectory optimization of a reciprocating compressor. *Int. J. Refrig.* **2021**, *121*, 159–167. [CrossRef]
7. Taleb, A.I.; Barfuß, C.; Sapin, P.; White, A.J.; Fabris, D.; Markides Christos, N. Simulation of thermally induced thermodynamic losses in reciprocating compressors and expanders: Influence of real-gas effects. *Appl. Therm. Eng.* **2022**, *217*, 118738. [CrossRef]
8. Patil, V.C.; Ro, P.I. Experimental study of heat transfer enhancement in liquid piston compressor using aqueous foam. *Appl. Therm. Eng.* **2020**, *164*, 114441. [CrossRef]
9. Patil, V.C.; Liu, J.; Ro, P.I. Efficiency improvement of liquid piston compressor using metal wire mesh for near-isothermal compressed air energy storage application. *J. Energy Storage* **2020**, *28*, 101226. [CrossRef]
10. Neu, T.; Solliec, C.; Piccoli, B.d.S. Experimental study of convective heat transfer during liquid piston compressions applied to near isothermal underwater compressed-air energy storage. *J. Energy Storage* **2020**, *32*, 101827. [CrossRef]
11. Patil, V.C.; Acharya, P.; Ro, P.I. Experimental investigation of heat transfer in liquid piston compressor. *Appl. Therm. Eng.* **2019**, *146*, 169–179. [CrossRef]
12. Niazmand, A.; Farzaneh-Gord, M.; Deymi-Dashtebayaz, M. Exergy analysis and entropy generation of a reciprocating compressor applied in CNG stations carried out on the basis models of ideal and real gas. *Appl. Therm. Eng.* **2017**, *124*, 1279–1291. [CrossRef]
13. Farzaneh-Gord, M.; Niazmand, A.; Deymi-Dashtebayaz, M.; Rahbari, H.R. Thermodynamic analysis of natural gas reciprocating compressors based on real and ideal gas models. *Int. J. Refrig.* **2015**, *56*, 186–197. [CrossRef]
14. Silva, L.R.; Deschamps Cesar, J. Modeling of gas leakage through compressor valves. *Int. J. Refrig.* **2015**, *53*, 195–205. [CrossRef]
15. Wang, Y.; Ren, P.; Xiong, W.; Peng, X. Strain analysis and non-destructive monitoring of the two-stage hydraulic-driven piston compressor for hydrogen storage. *J. Energy Storage* **2024**, *94*, 112494. [CrossRef]
16. Kong, F.; Tang, M.; Zou, H.; Zhang, S.; Hu, Z.; Tian, C. Performance simulation analysis of a novel dual-piston two-stage carbon dioxide linear compressor. *Int. J. Refrig.* **2024**, *159*, 185–194. [CrossRef]
17. Ye, J.; He, Y.; Du, Z.; Ji, R.; Xie, J.; Liu, J. The transient flow and heat transfer characteristics in reciprocated conditions of hydraulic-driven piston hydrogen compressor in hydrogen storage system. *J. Energy Storage* **2024**, *89*, 111662. [CrossRef]
18. Wu, W.; Guo, T.; Peng, C.; Li, X.; Li, X.; Zhang, Z.; Xu, L.; He, Z. FSI simulation of the intake valve on the piston for reciprocating compressors. *Int. J. Refrig.* **2022**, *137*, 14–21. [CrossRef]
19. Zhou, H.; Dong, P.; Zhu, S.; Li, S.; Zhao, S.; Wang, Y. Design and theoretical analysis of a liquid piston hydrogen compressor. *J. Energy Storage* **2021**, *41*, 102861. [CrossRef]
20. Xu, W.; Du, Z.; Wang, X.; Cai, M.; Jia, G.; Shi, Y. Isothermal piston gas compression for compressed air energy storage. *Int. J. Heat Mass Transf.* **2020**, *155*, 119779. [CrossRef]
21. Han, Z.; Liu, S.; Li, P.; Yang, P.; Shang, H. Dynamic simulation and structural analysis of improved adiabatic compressed air energy storage system based on liquid piston. *J. Energy Storage* **2024**, *101*, 113737. [CrossRef]
22. Wang, Y.; Jiang, Z.; Zhang, J.; Zhou, C.; Liu, W. Performance analysis and optimization of reciprocating compressor with stepless capacity control system under variable load conditions. *Int. J. Refrig.* **2018**, *94*, 174–185. [CrossRef]
23. Gao, G.; Wu, H.; Sun, L.; He, L. Comprehensive Quality Evaluation System for Manufacturing Enterprises of Large Piston Compressors. *Procedia Eng.* **2017**, *174*, 566–570. [CrossRef]
24. Hu, Z.; Li, J.; Tan, H. Helium screw compressor for 5tpd large-scale hydrogen liquefier. *Cryogenics* **2024**, *141*, 103890. [CrossRef]
25. Wang, T.; Qi, Q.; Zhang, H.; Wang, B.; Peng, X. Investigation on dynamic stress of the discharge valve in the transcritical CO_2 compressor. *Renew. Energy* **2024**, *220*, 119589. [CrossRef]
26. Zhi, X.; Cao, R.; Jiang, X.; You, X.; Qiu, L. Study on the output pressure amplitudes of the linear compressor based on the complex vector analysis method. *Int. J. Refrig.* **2019**, *107*, 355–364. [CrossRef]
27. Ma, J.; Ding, X.; Horton, W.T.; Ziviani, D. Development of an automated compressor performance mapping using artificial neural network and multiple compressor technologies. *Int. J. Refrig.* **2020**, *120*, 66–80. [CrossRef]

28. Taranović, D.; Ninković, D.; Davinić, A.; Pešić, R.; Glišović, J.; Milojević, S. Valve dynamics in reciprocating compressors for motor vehicles. *Teh. Vjesn.* **2017**, *24*, 313–319. [CrossRef]
29. Milojević, S.; Džunić, D.; Marić, D.; Skrúcaný, T.; Mitrović, S.; Pešić, R. Tribological assessment of aluminum cylinder material for piston compressors in trucks and buses brake systems. *Teh. Vjesn.* **2021**, *28*, 1268–1276. [CrossRef]
30. Liu, Y.; Yan, H.; Liu, Y.; Lu, L.; Li, Q. Numerical study of corner separation in a linear compressor cascade using various turbulence models. *Chin. J. Aeronaut.* **2016**, *29*, 639–652. [CrossRef]
31. Sun, W. Assessment of advanced RANS turbulence models for prediction of complex flows in compressors. *Chin. J. Aeronaut.* **2023**, *36*, 162–177. [CrossRef]
32. Pang, H.; Zhang, Y.; Xu, L.; Li, B.; Zhang, L.; Song, M.; Tang, S. Comparative analysis of lubrication characteristics between variable eccentricity and constant eccentricity of oil film in a floating ring bearing. *Lubr. Eng.* **2022**, *47*, 92–98. [CrossRef]
33. Ye, J.-G.; Xu, S.-S.; Huang, H.-F.; Zhao, Y.-J.; Zhou, W.; Zhang, Y.-L. Optimization design of nozzle structure inside boiler based on orthogonal design. *Processes* **2023**, *11*, 2923. [CrossRef]
34. Baker, N.; Kelly, G.; O'Sullivan, P.D. A grid convergence index study of mesh style effect on the accuracy of the numerical results for an indoor airflow profile. *Int. J. Vent.* **2020**, *19*, 300–314. [CrossRef]

Disclaimer/Publisher's Note: The statements, opinions and data contained in all publications are solely those of the individual author(s) and contributor(s) and not of MDPI and/or the editor(s). MDPI and/or the editor(s) disclaim responsibility for any injury to people or property resulting from any ideas, methods, instructions or products referred to in the content.